1.0

1.1

1.25 1.4 1.6

4.5
5.0

2.8 2.5
3.2 2.2
3.6
4.0 2.0

1.8

MICROCOPY RESOLUTION TEST CHART
NATIONAL BUREAU OF STANDARDS-1963-A

ADA085448

STUDIES OF TRANSIONOSPHERIC SCINTILLATION USING
ORBITING SATELLITE DATA

Stanley Brittain Quinn, Jr.

Department of Electrical Engineering
University of Illinois at Urbana-Champaign
Urbana, Illinois 61801

April 1980

Scientific Report, No. 2

Approved for public release; distribution unlimited.

AIR FORCE GEOPHYSICS LABORATORY
AIR FORCE SYSTEMS COMMAND
UNITED STATES AIR FORCE
HANSCOM AFB, MASSACHUSETTS 01731

80 6 13 034

REPORT DOCUMENTATION PAGE	READ INSTRUCTIONS BEFORE COMPLETING FORM

1. REPORT NUMBER	2. GOVT ACCESSION NO.	3. RECIPIENT'S CATALOG NUMBER
AFGL-TR-80-0092	AD-A085 448	

4. TITLE (and Subtitle)	5. TYPE OF REPORT & PERIOD COVERED
Studies of Transionospheric Scintillation Using Orbiting Satellite Data	Scientific report No. 2. Jul 79 — Jul 80
	6. PERFORMING ORG. REPORT NUMBER
	TR No. 66, UILU-ENG-80-2539

7. AUTHOR(s)	8. CONTRACT OR GRANT NUMBER(s)
Stanley Brittain Quinn, Jr.	F19628-78-C-0195

9. PERFORMING ORGANIZATION NAME AND ADDRESS	10. PROGRAM ELEMENT, PROJECT, TASK AREA & WORK UNIT NUMBERS
Department of Electrical Engineering University of Illinois at Urbana-Champaign Urbana, Illinois 61801	63431F 464305AA 05

11. CONTROLLING OFFICE NAME AND ADDRESS	12. REPORT DATE
Air Force Geophysics Laboratory (PHP) Hanscom AFB, Massachusetts 01731 Monitor/Herbert E. Whitney/PHP	Apr 80
	13. NUMBER OF PAGES
	72

14. MONITORING AGENCY NAME & ADDRESS(if different from Controlling Office)	15. SECURITY CLASS. (of this report)
73	UNCLASSIFIED
	15a. DECLASSIFICATION/DOWNGRADING SCHEDULE

16. DISTRIBUTION STATEMENT (of this Report)

Approved for public release; distribution unlimited.

UILU-ENG-80-2539, TR-66

17. DISTRIBUTION STATEMENT (of the abstract entered in Block 20, if different from Report)

18. SUPPLEMENTARY NOTES

Contract F19628-78-C-0195 is supported by Hq. Space Division, YKX, Los Angeles, CA. 90009

19. KEY WORDS (Continue on reverse side if necessary and identify by block number)

Transionospheric radio propagation
Ionospheric scintillation
Weak and strong scintillation

20. ABSTRACT (Continue on reverse side if necessary and identify by block number)

Multi-frequency studies of transionospheric radio signals fluctuations are facilitated by the DNA Wideband Satellite Experiment run by SRI International. Mutually coherent signals were recorded at equatorial, mid-latitude and auroral stations. Results including statistical parameters of the received signals as well as what they reveal about the ionosphere are discussed. Correlations and power spectra of the signals are also computed.

DD FORM 1473
1 JAN 73
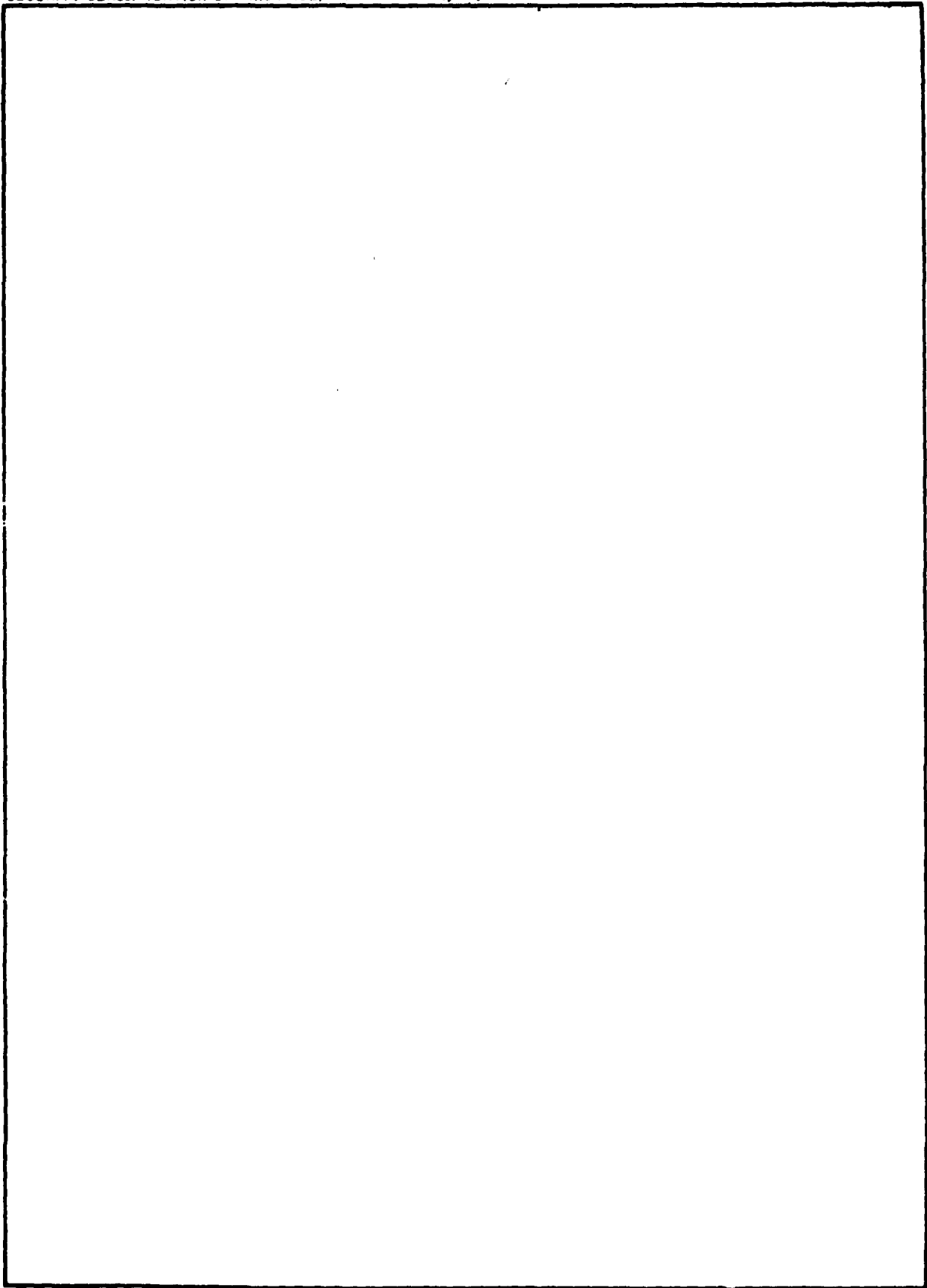
ACKNOWLEDGEMENT

My deepest gratitude is extended to Dr. C. H. Liu and Dr. K. C. Yeh of the Ionosphere Radio Laboratory for the opportunity to carry out this work and their conscientious guidance throughout. Likewise, I am indebted to Bob Livingston, Chuck Rino and Stu Stephens of SRI International for their assistance in obtaining the data used for this research. In addition, I would like to thank Mrs. Linda Houston for typing this manuscript as well as providing other invaluable assistance in its production. Finally, thanks are in order for Dr. J. Beauchamp and Dr. H. Thompson for their friendship and inspiration.

TABLE OF CONTENTS

LIST OF TABLES

LIST OF FIGURES

LIST OF FIGURES CONT.

1. Introduction

For the most part, the atmosphere provides a reliable media for signal propagation in radio communications systems. It is largely homogeneous and can be modelled as free space for most situations. When signals pass through the ionosphere, however, a great deal of complications arise.

Radio waves undergo scattering in a structured plasma, as in the ionosphere. The resultant perturbations imposed on the signal can prove deleterious in a communications system. Temporal fluctuations in the received signal translate into distortion after demodulation. Both amplitude fading and phase fluctuations affect various types of systems.

In order to characterize these fluctuations, continuous wave signals are transmitted by satellite and received on the ground after passing through the ionosphere. In this report, data from the DNA wideband satellite experiment were obtained at various stations around the world run by SRI International. The received complex signal displays the variation of the transionospheric scintillations.

By studying the temporal structure of the ampltide and phase scintillations insight can be gained into the structure of the irregularities. The actual data available are from low, medium and high latitudes. At equatorial and auroral latitudes there is considerable ionospheric activity contributing to extensive scintillation. Close scrutiny is given to these data sets.

In addition to interpreting the scintillation data in terms of geophysical parameters in the ionosphere (such as mean square deviation of electron density, the irregularity spectrum, etc.) the statistical studies of the scintillation data can also yield information that is

useful to communication engineers. For example, the high frequency
asymptote of the amplitude power spectrum is found to follow a power
law of the form ν^{-n}, which predicts a frequency dependence of the S_4
scintillation index in the form $f^{-(n+3)/4}$ in the weak scatter regime.
Thus if n is determined experimentally, the dependence of scintillation
on radio frequency f is known at least when the scintillation is not
strong. As an another example, the value of correlation time is a
desirable information to have in applications of time diversity. If
the temporal variation in the signal is created by drifting of frozen-
in random field as usually is the case, the correlation time can be
easily translated to the spatial correlation interval. Of course,
in applications of spatial diversity it is desirable to know the value
of spatial correlation interval. The four ground stations from which
data were collected are Poker Flat, Alaska (auroral station), Stanford,
California (mid-latitude station), and Ancon, Peru and Kwajalein, Marshall
Island (both equatorial stations). In the natural environment there is
least scintillation at mid-latitude, followed by the auroral station.
The equatorial stations have the strongest scintillation. Consequently,
in this sense the equatorial environment is the closest simulation to
the case of artificially modified ionosphere.

Previous work in this area has been carried out with a different type
of data. Umeki et al. (1977a,b) and Myers (1979) used data from the ATS-6
Radio Beacon Experiments. Frequency coverage in this data was limited to
40, 140, and 360 MHz, with the latter providing the phase reference. In
addition, the satellite was geostationary and the data analyzed provided
temporal latitude coverage only. Orbiting satellite data at many frequencies
from diverse geographic locations is used here to overcome these limitations.

Previous studies of the SRI data have also been carried out. Fremouw et al. (1977) undertook studies using large amounts of data to draw general conclusions. In this report specific data sets will be examined extensively in "case study" analysis.

Chapter 2 gives some motivation for the subsequent studies by predicting the theoretical bases for scintillation. Weak and strong scintillation, including a general theory on the autocorrelation of the complex signal, are examined. Chapter 3 is devoted to the techniques used in acquisition and analysis of the data. Results and conclusions are then presented in chapters 4 and 5, respectively.

2.   Scintillation Theory

In this chapter, some of the physics of a model ionosphere will be discussed in order to develop predictions about its behavior.

2.1 Weak Scintillation

For our purpose of scintillation study, the ionosphere can be thought of as a slab with thickness L containing electron density irregularities conducive to the scattering of radio waves. An orbiting satellite's transmissions are received at an earth station, thus exhibiting the effects of spatial variations in the slab (Fig. 2.1.1). The electric field in the slab is given by the solution of the inhomogeneous wave equation.

$$\nabla^2\vec{E}+k^2\epsilon(\vec{r})\vec{E} = -\nabla(\vec{E}\cdot\nabla\ell n[\epsilon(\vec{r})])\qquad(2.1.1)$$

$$k = \frac{2\pi}{\lambda}, \qquad \lambda = \text{wavelength}$$

$$\epsilon = \text{dielectric permittivity}$$

Because compared to the velocity of the radio signal (as well as the satellite) the variations in the irregularity change very slowly, the permittivity can be considered a function of position only. It can be formulated as

$$\epsilon(\vec{r}) = <\epsilon>[1+\epsilon_1(\vec{r})]\qquad(2.1.2)$$

where $\epsilon_1(\vec{r})$ is the random component of the permittivity.

For weak scintillation, or single scattering, the Rytov approximation can be applied (Tatarski, 1971). For a large distance between the transmitter and the top of the slab, plane wave incidence of the form $\vec{E}_0\exp(-j\vec{k}\cdot\vec{r})$ can be assumed. This gives a Rytov solution to (2.1.1) as (Tatarski, 1971)

Transmitter

$(z \rightarrow -\infty)$

z = 0

L

z = L

Receiver at (0,0,z)
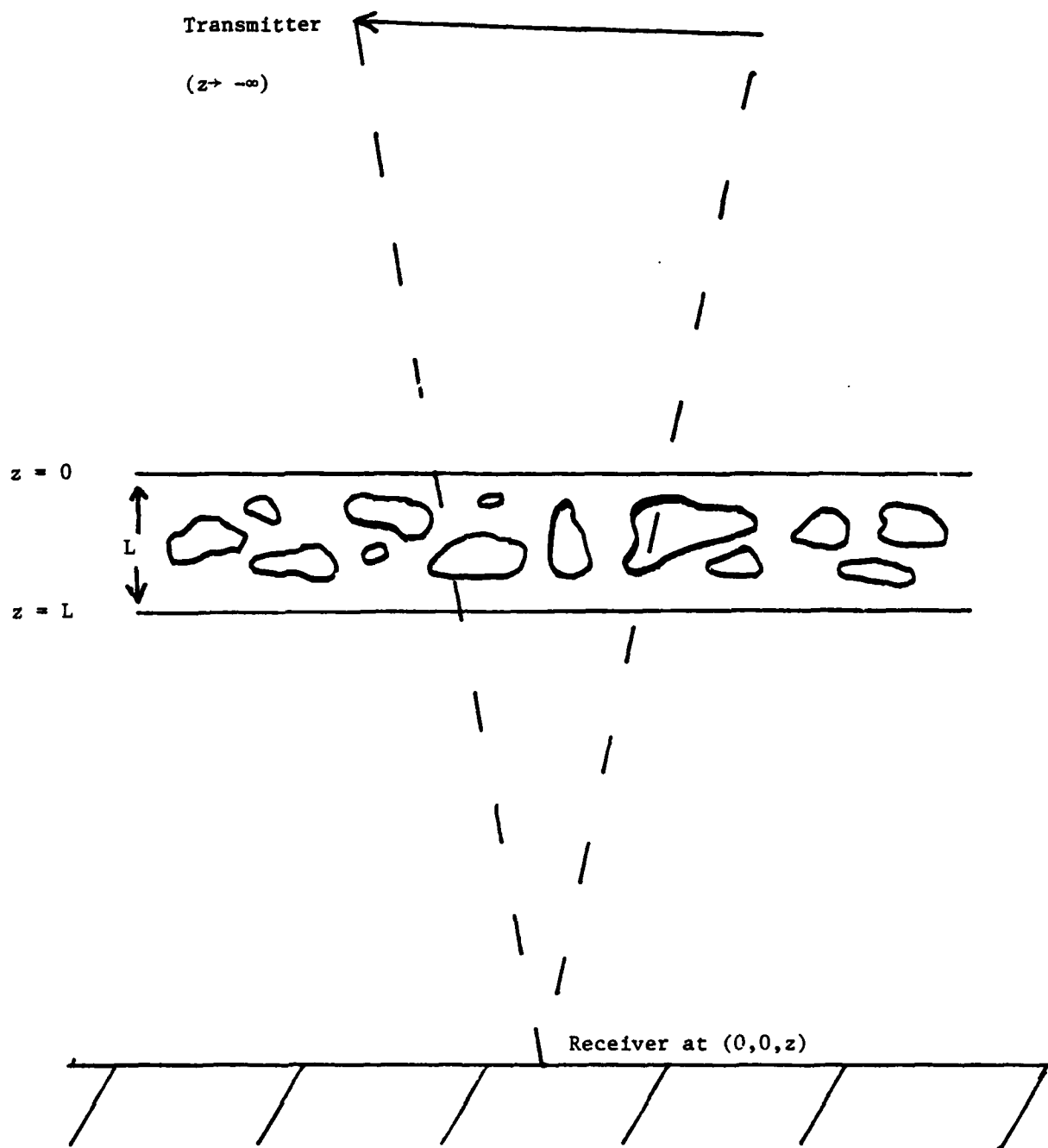
Figure 2.1.1 Geometry of Model.

$$\vec{E}(\vec{r}) = \vec{E}_0 \exp(-j\vec{k}\cdot\vec{r}+\psi(\vec{r})), \tag{2.1.3}$$

$$\psi(\vec{r}) = r_e \iiint \Delta N_e(\vec{r}\,')\exp[j\vec{k}\cdot(\vec{r}-\vec{r}\,')]\exp[jk|\vec{r}-\vec{r}\,'|]\left(\frac{d\vec{r}\,'}{|\vec{r}-\vec{r}\,'|}\right)$$

r_e = classical electron radius

ΔN_e = electron density fluctuation

The complex quantity, $\psi(\vec{r})$, can be written as the sum of its real and imaginary components.

$$\psi(\vec{r}) = \chi(\vec{r})+jS(\vec{r}) \tag{2.1.4}$$

The real part, χ, will yield amplitude variations while the imaginary component, S, represents the phase fluctuations.

It has been shown (Wernik et al., 1973) that at the receiver on the ground

$$\langle\chi^2\rangle = \frac{\pi^2 k^2 L}{2}\left[\frac{f_p}{f_t}\right]^4 \int_0^\infty F_F(\kappa)\Phi_N(\kappa)\kappa d\kappa,$$

$$\tag{2.1.5}$$

$$F_F(\kappa) = 1 - \frac{2k}{\kappa^2 L}\sin\left(\frac{\kappa^2 L}{2k}\right)\cos\left[\frac{\kappa^2}{k}\left(z - \frac{L}{2}\right)\right]$$

and also

$$\langle S^2\rangle = \frac{\pi^2 k^2 L}{2}\left[\frac{f_p}{f_t}\right]^4 \int_0^\infty F_\phi(\kappa)\Phi_N(\kappa)\kappa d\kappa,$$

$$\tag{2.1.6}$$

$$F_\phi(\kappa) = 1 + \frac{2k}{\kappa^2 L}\sin\left(\frac{\kappa^2 L}{2k}\right)\cos\left[\frac{\kappa^2}{k}\left(z - \frac{L}{2}\right)\right]$$

where

κ = spatial wave number

$\Phi_N(\kappa)$ = power spectrum of electron density fluctuations

f_t = signal frequency

f_p = plasma frequency of background ionosphere

Experimentally (Rufenach, 1972; Crane, 1976), a power law spectrum has been demonstrated for the irregularities; i.e., $\Phi_N \propto \kappa^{-p}$. The specific form used is

$$\Phi_N(\vec{\kappa}) = \frac{<(\Delta N/N_0)^2> \eta r_0^3 \; \Gamma(p/2)}{2\pi\Gamma(3/2)\Gamma(\frac{p-3}{2})[1+r_0^2(\kappa_x^2+\eta^2\kappa_y^2)]^{p/2}} \qquad (2.1.7)$$

$<(\Delta N/N_0)^2>$ = variance of electron density fluctuations

η = anisotropy factor

r_0 = outer scale size of irregularities

$\Gamma(x)$ = gamma function

The temporal power spectra of the received signal can now be predicted. Assuming frozen-in irregularities, Umeki et al. (1976) gave an amplitude spectrum of

$$P_A(\Omega) = \frac{\pi k^2 L}{4v} \; (\frac{f_p}{f_t})^4 \int_{-\infty}^{\infty} F_F(q)\Phi_N(\vec{\kappa})d\kappa_y \qquad (2.1.8)$$

The phase spectrum is (Singleton, 1974)

$$P_\Phi(\Omega) = \frac{\pi k^2 L}{4v} \; [\frac{f_p}{f_t}]^4 \int_{-\infty}^{\infty} F_\Phi(q)\Phi_N(\vec{\kappa})d\kappa_y \qquad (2.1.9)$$

where $\Omega = 2\pi f$

$q^2 = \frac{\Omega^2}{v^2} + \kappa_y^2$

f = temporal frequency

v = satellite velocity, projected onto slab

For amplitude, the temporal spectrum begins to roll off at the Fresnel frequency, $f_F = v/\lambda_F$. Given the condition of power law irregularity spectrum, the temporal amplitude power spectrum will decrease as $f^{-(p-1)}$ at the high frequency end. On the other hand, the temporal phase spectrum should be

proportional to $f^{-(p-1)}$ for all frequencies above the cutoff used to detrend the data. The low frequency leveling-off characteristic of the amplitude spectrum is due to the Fresnel filtering effect. Irregularities larger than the Fresnel size $(\lambda_F = \sqrt{\lambda(2z-L)})$ do not contribute significantly to amplitude scintillation.

2.2 Strong Scintillation

The above derivations are valid only under the conditions $|\varepsilon_1| \ll 1$, $\langle\chi^2\rangle \ll 1$, and $\langle S^2 \rangle \ll 1$. These no longer hold for strong scintillations. Multiple scattering effects present an extremely complicated situation. Rumsey (1975) and Marians (1975) have carried out some theoretical computations for the amplitude spectrum using a phase screen model. Their results predict that, even under conditions of strong scintillation, the power spectrum will roll off with a constant slope. Liu et al., (1974) and Yeh et al., (1975) have studied the saturation effects of the amplitude scintillation, frequency dependence of scintillation index and the correlation time under multiple scattering conditions. Some of those results will be applied to the interpretation of the data.

2.3 Correlation Characteristics

Some current theoretical investigations are predicting behavior that applies both in strong and weak cases. In particular, both the average field and the mutual coherence function of the field can be obtained analytically under the forward scatter approximation.

Let us define the complex amplitude of the field, U, by $E = U\exp(-jkz)$. Insight can be gained into the actual structure of the irregularities by observing the autocorrelation of the received signal, $U(z,\rho)|z$=ground. The mutual coherence function of the complex amplitude is defined as

$$\Gamma_2 = <U(z,\vec{\rho}_1)U^*(z,\vec{\rho}_2)> \qquad (2.3.1)$$

For plane wave incidence a solution can be obtained for both $<U>$ and Γ_2 (Tatarski, 1971) inside the irregularity slab:

$$<U> = U_0\exp[-\frac{k^2z}{8} A(0)] \qquad (2.3.2)$$

$$\Gamma_2 = U_0{}^2\exp\{-\frac{k^2z}{4} [A(0)-A(\vec{\rho})]\}, \qquad (2.3.3)$$

$A(\vec{\rho})$ = 2 dimensional correlation function

for ε_1 irregularities

$$= \int_{-\infty}^{\infty} B\varepsilon(\vec{\rho},z)dz$$

U_0 = incident field amplitude

Below the slab, $z>L$, the results are

$$\Gamma_2 = U_0{}^2\exp\{-\frac{k^2L}{4} [A(0)-A(\vec{\rho})]\} \qquad (2.3.4)$$

$$<U> = U_0\exp[-\frac{k^2L}{8}A(0)] \qquad (2.3.5)$$

Define $L=\ln[\Gamma_2/<U>^2]$ and hence

$$L = \ln\Gamma_2-\ln<U>^2 \qquad (2.3.6)$$

Substitution of (2.3.4) and (2.3.5) in (2.3.6) yields

$$L(\vec{\rho}) = \frac{k^2L}{4} A(\vec{\rho}) \qquad (2.3.7)$$

In terms of the percentage electron density fluctuation $\Delta N/N_0$, (2.3.7) can be written as

$$L(\vec{\rho}) = \frac{\pi^2 f_p^{\,4} L}{c^2 f_t^{\,2}} A_N(\vec{\rho}),\tag{2.3.8}$$

c = speed of light

A_N = two-dimensional transverse correlation function of $\Delta N/N_0$

Assuming "frozen in" irregularities (Tatarski, 1971), the transverse displacement becomes $\vec{\rho} = \vec{v}t$. Thus, the correlation of the irregularities can be observed directly from the logarithm of the correlation of the received complex signal.

In terms of the irregularity spectrum, Φ_N, $A_N(\vec{v},t)$ can be formulated as

$$A_N(\vec{v},t) = 2\pi \iint \Phi_N(0,\vec{\kappa}) e^{-j\vec{\kappa}\cdot\vec{v}t} d\vec{\kappa}\tag{2.3.9}$$

Next we evaluate the temporal spectrum of $A_N(\vec{v},t)$

$$\int A_N(v,t) e^{j\Omega t}\, dt = 2\pi \iint \Phi_N(0,\vec{\kappa})\, d\vec{\kappa} \int e^{j(\Omega - \vec{\kappa}\cdot\vec{v})t}\, dt$$

$$= 4\pi^2 \iint \Phi_N(0,\vec{\kappa}) d\vec{\kappa}\, \delta(\Omega - \vec{\kappa}\cdot\vec{v})\tag{2.3.10}$$

$$= 4\pi^2 I$$

Let $\kappa_y v_y = y$, $\kappa_y = \dfrac{y}{v_y}$, $d\kappa_y = \dfrac{dy}{v_y}$ then I becomes

$$I = \iint \Phi_N(0,\kappa_x,\kappa_y)\, \delta(\Omega - \kappa_x v_x - y) d\kappa_x d\kappa_y$$

$$= \iint \Phi_N(0,\kappa_x, \frac{y}{v_y})\, \delta(\Omega - \kappa_x v_x - y) d\kappa_x dy/v_y\tag{2.3.11}$$

$$= \frac{1}{v_y} \int \Phi_N(0,\kappa_x, \frac{\Omega - \kappa_x v_x}{v_y})\, d\kappa_x$$

Further evaluation depends on the behavior of Φ_N. As an example, let us consider the case of isotropic irregularities such that (2.1.7) reduces to

$$\Phi_N = C_n (1 + r_0^2 \kappa^2)^{-(\nu + \frac{1}{2})}, \tag{2.3.12}$$

$$\nu = \frac{(P-1)}{2}$$

$$C_N = \frac{\langle (\Delta N/N_0)^2 r_0^3 \Gamma(p/2) \rangle}{2\pi \Gamma(3/2) \Gamma(\frac{p-3}{2})}$$

Furthermore, let us assume, without loss of generality, that all velocity is in the y direction ($v_x = 0$). This gives

$$\Phi_N(0, \kappa_x, \frac{\Omega - \kappa_x v_x}{v_y}) = C_N [1 + \frac{r_0^2 \Omega^2}{v_y^2} + r_0^2 \kappa_x^2]^{-(\nu + \frac{1}{2})} \tag{2.3.13}$$

and (2.3.11) becomes

$$I = \frac{C_N}{v_y} \int_{-\infty}^{\infty} (1 + \frac{r_0^2 \Omega^2}{v_y^2} + r_0^2 \kappa_x^2)^{-(\nu + \frac{1}{2})} d\kappa_x$$

$$\tag{2.3.14}$$

$$= \frac{2^\nu C_N}{r_0 v_y} \left(\frac{(\nu-1)!}{(2\nu-1)!!}\right) (1 + \frac{r_0^2 \Omega^2}{v_y^2})^{-\nu}$$

where ν is assumed to be an integer and $(2\nu-1)!! = 1 \cdot 3 \cdot 5 \ldots \cdot (2\nu-1)$. From (2.3.8), (2.3.10) and (2.3.14) we can compute the spectrum of L.

$$P_L = \frac{\pi^2 f_p^4 L}{c^2 f_t^2} \int A_N(\vec{v}, t) e^{j\Omega t} dt$$

$$\tag{2.3.15}$$

$$= \frac{4\pi^2 f_p^4}{c^2 f_t^2} (\frac{C_N}{v_y}) (\frac{2^\nu}{r_0}) (\frac{(\nu-1)!}{(2\nu-1)!!}) (1 + \frac{\Omega^2 r_0^2}{v_y^2})^{-\nu}$$

Thus, for isotropic irregularities, the power spectrum of the quantity L defined in (2.3.7) yields direct information about the spectral shape of

the density fluctuations. For a more general case, (2.3.11) can be evaluated.

These theoretical results for both weak and strong scintillations will be used later in the thesis for purposes of data interpretation.

3. Data Acquisition and Processing

In this section the techniques used for acquisition and analysis of the data will be explored.

3.1 Design of Experiment

In May of 1976 Stanford Research Institute initiated the DNA Wideband Satellite Experiment for the Defense Nuclear Agency. Satellite P76-5 was launched into a 1000 km near-polar orbit. The satellite carried a multi-frequency coherent transmitter radiating 10 CW signals ranging from VHF to S-band (Table 3.1.1). The program was designed to study the scintillations of radio waves induced by the ionosphere (Fremouw, et al., 1978).

TABLE 3.1.1 Data Channel Frequencies

Channel	Frequency MHz	Harmonic (of 11.4729 MHz)
VHF	137.6748	12
UL3	378.6057	33
UL2	390.0786	34
UL1	401.5515	35
UC	413.0244	36
UU1	424.4973	37
UU2	435.9702	38
UU3	447.4431	39
L-band	1239.073	108
S-band	2891.171	252

Data was collected at four ground stations. At mid-latitudes, a receiver was located at Stanford, California. For equatorial observations, stations were located at Ancon, Peru (near Lima) and Kwajalein atoll in the Marshall

Islands. Study of auroral behavior was facilitated by a receiver at the Poker
Flat Rocket Range near Fairbanks, Alaska (Table 3.1.2).

TABLE 3.1.2 Ground Station Locations

station	Geodetic Coordinates latitude	longitude	Geomagnetic dip latitude
Poker Flat, Alaska	65°7'34"N	147°29'14"W	65.4°N
Ancon, Peru	11°46'34"S	77°9'00"W	0.4°N
Kwajalein, Marshall Islands	9°24'08"N	167°28'10"E	4.4°N
Stanford, California	37°24'10"N	122°10'27"W	42.8°N

The receivers are designed to yield a signal at the differential doppler
frequency between the appropriate measured signal and the S-band reference
(Fig. 3.1.1). A synthesizer, phase-locked to the reference phase, provides
quadrature outputs to the measured signals phase detectors. These (x,y) out-
puts are bandlimited to 150 Hz, digitized, and recorded at 500 samples per
second.

Initial processing is performed in the field. The data is decimated to
100 Hz samples and converted to intensity and phase. In order to remove trends
due to TEC a detrending procedure is applied. First, the intensity and phase
are smoothed by a 0.1 Hz (ten second) 6-pole Butterworth low-pass filter. De-
trended intensity is obtained by evaluating the quotient of the original signal
and its trend. The detrended phase results from subtracting the trend from
the raw data. The data are then scaled to give unity mean intensity and zero
mean phase (Fig. 3.1.2). These signals are then recorded on nine-track tape.
Associated summary tapes are also generated containing second order signal
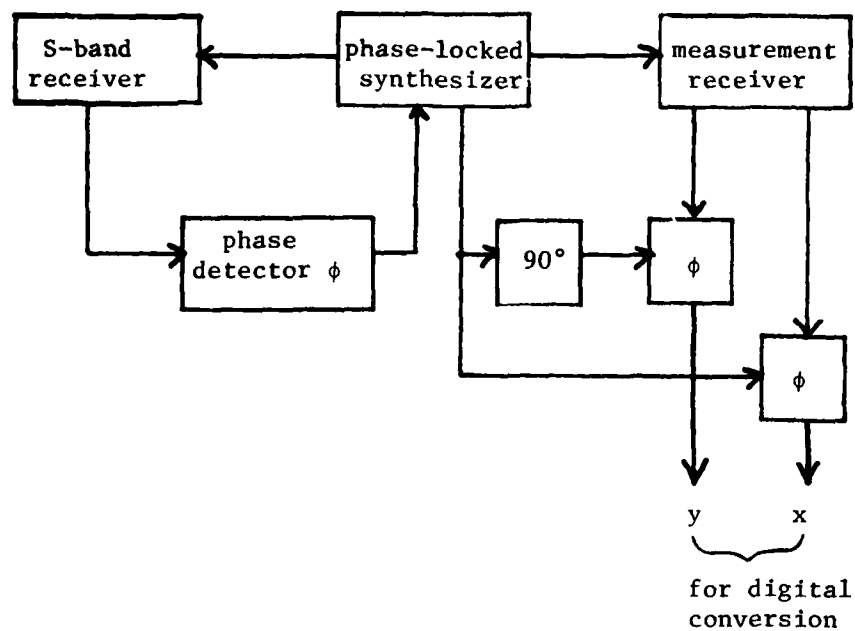statistics and geometry information on the satellite pass.

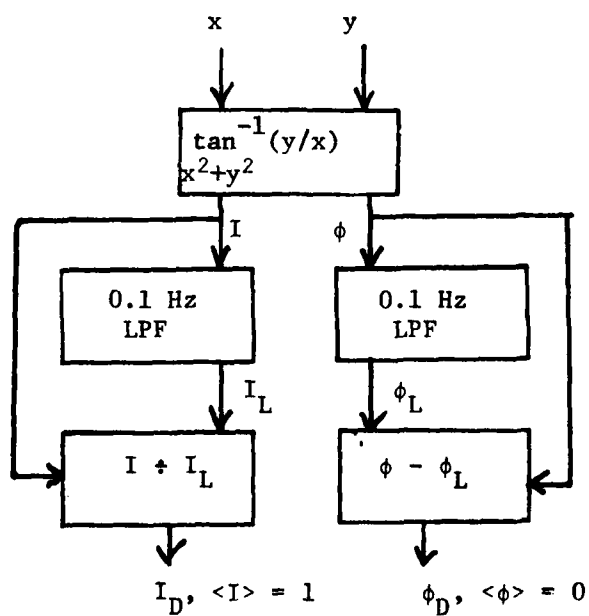Fig. 3.1.1   Coherent Receiver for One Measurement Channel

Fig. 3.1.2   Detrending Procedure

After examining strip charts and signal statistics, several of these tapes were copied from the SRI data library. Each tape contains one satellite pass of approximately fifteen minutes. The ten second detrended tapes contain nine channels of information: three files with three channels each. The channel frequencies used, available from each station, were 137.7 MHz (VHF), 378.6 MHz and 447.5 MHz (UHF), 1239.1 MHz (L-band) and 2891.2 MHz (S-band). For each pass copied, the corresponding summary tape was also copied.

3.2 Initial Conversion

Before the data could be useful, it had to be converted to a form accessible to the Cyber 175 at the University of Illinois. This conversion involved essentially two tasks. The numerical values had to be unpacked and converted from SRI's (Hewlett-Packard) formats to the data representations appropriate for the Cyber. In addition, the file/record structure was organized into a more useful form.

The HP formatted data consists of two's compliment integers and double-precision floating point words (Fig. 3.2.1). Each word contains 16 data bits. The conversion process maps these to 60 bit one's compliment integers and floating point Cyber words (Fig. 3.2.2).

The format of the ten second detrended tapes obtained from SRI is cumbersome. For the computations in the subsequent analyses it is necessary to have the data files divided by frequency and subdivided into magnitude and phase. The SRI format intermixes the different frequencies (channels) and their respective magnitudes and phases (Fig. 3.2.3) within each record.

The amplitude (magnitude) of the signal is more useful for our purposes than the intensity. This is computed by taking the positive square root of the intensity. Because of the very large number of data points, they were
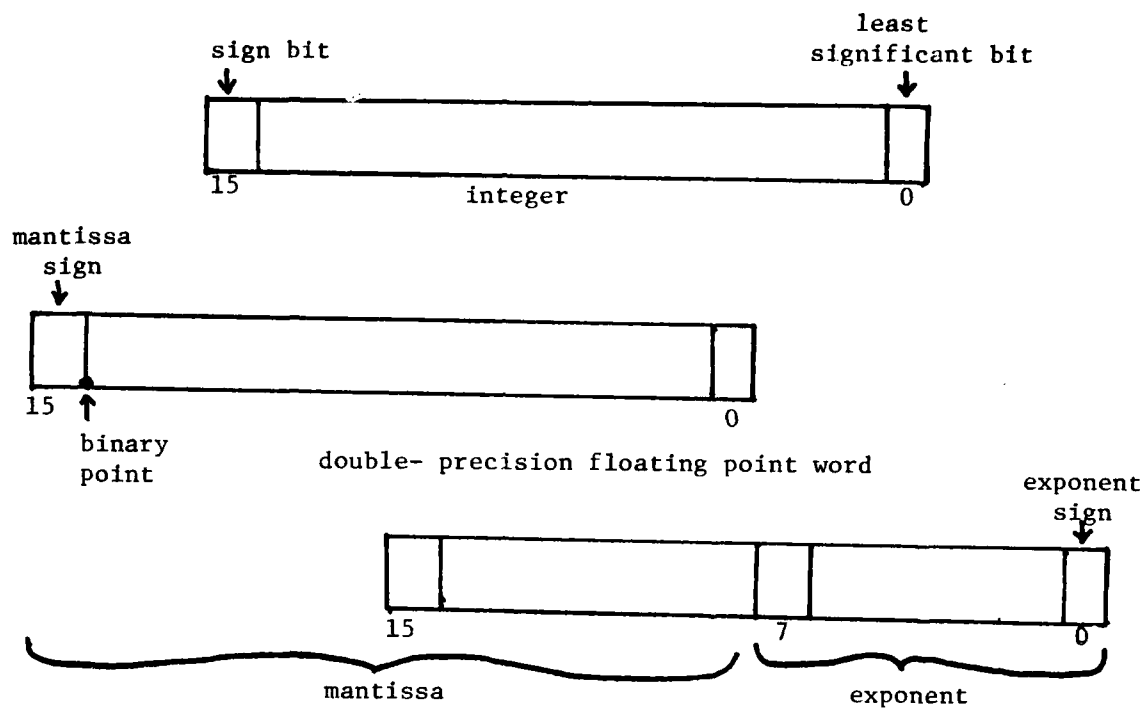
17

sign bit   least
                                   significant bit

15   integer   0

mantissa
sign

15   0

binary
point   double- precision floating point word

                                                exponent
                                                sign

15   7   0

mantissa   exponent

Fig. 3.2.1 HP Numerical Representations

59   0

59 bit magnitude

sign   integer   least significant
                                       bit

59   47   0

11 bit biased   48 bit integer
exponent

real

sign   binary
                                              point
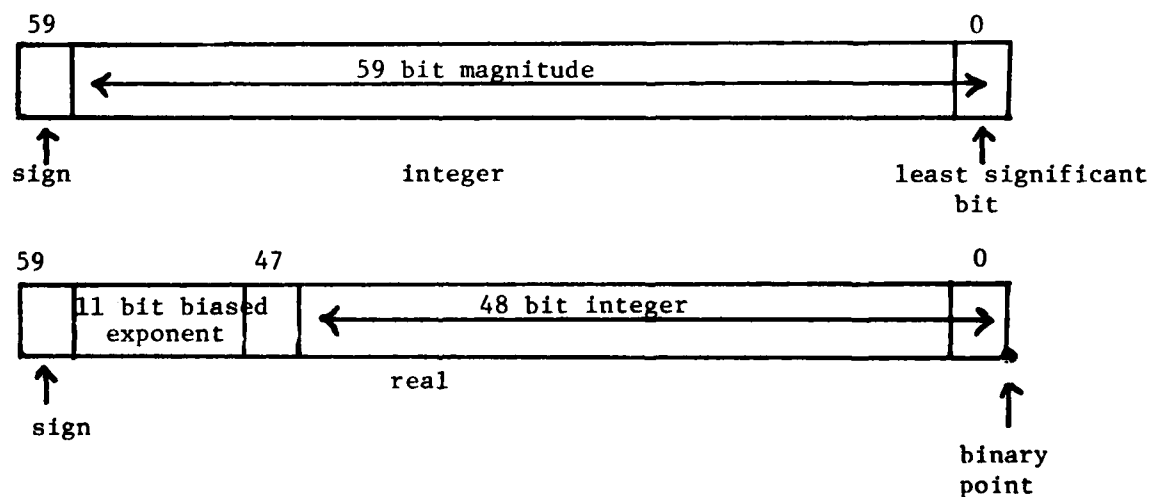
Fig. 3.2.2 Cyber Numerical Representations

records 1 and 2   duplicates of raw data records

records 3-end of file   (between 1000 and 2000 records):

word 1-2   intensity ⎫
                           ⎬ channel 1 ⎤
     3-4   phase   ⎭   │

     5-6   intensity ⎫   │
                           ⎬ channel 2 ⎬   double-precision floating
     7-8   phase   ⎭   │   point detrend values

     9-10   intensity ⎫   │
                           ⎬ channel 3 ⎦
     11-12   phase   ⎭

     13-600   repeat (50 times) above sequence

     601-720   low-pass reference signal

     721-727   time information

     728-729   antenna controller position

     730-742   blanks

Fig. 3.2.3.   SRI Format for 10-second detrend tapes used

split and recorded in records of 4000 points, maximum. Thus, an array of m points will occupy n records where

$$
n = \begin{cases} \dfrac{m}{4000} & , \; \text{mod}_{4000}(m) = 0 \\[2em] \dfrac{m}{4000} + 1 & , \; \text{mod}_{4000}(m) \neq 0 \end{cases}
\tag{3.2.1}
$$

The reformatted files, with separate amplitude and phase for separate channels, are in the form shown in Fig. 3.2.4. In any given file, however, one or two channels may be omitted if they are not needed.

records 1-n   amplitude $\left.\vphantom{\begin{array}{c}a\\b\end{array}}\right\}$ channel 1 $\left.\vphantom{\begin{array}{c}a\\b\\c\\d\\e\\f\end{array}}\right\}$
n+1-2n   phase

2n+1-3n   amplitude $\left.\vphantom{\begin{array}{c}a\\b\end{array}}\right\}$ channel 2   CYBER real values
3n+1-4n   phase

4n+1-5n   amplitude $\left.\vphantom{\begin{array}{c}a\\b\end{array}}\right\}$ channel 3
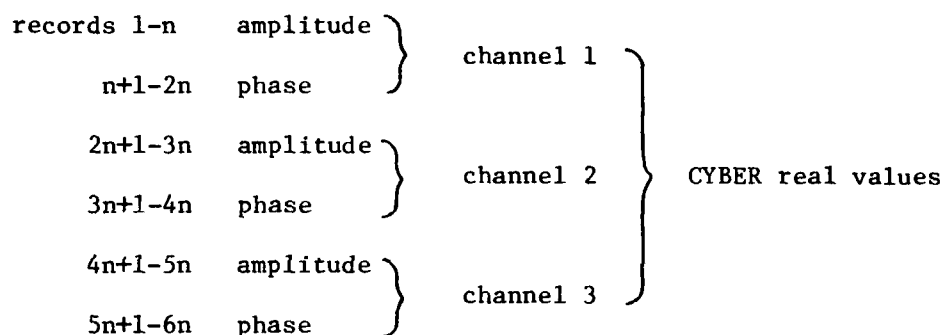5n+1-6n   phase

Fig. 3.2.4. Reformatted 10-second detrend file

The data sets are named through a simple procedure. Each satellite is referred to by the first letter of the receiving station and an ordinal index. K1 is the first pass recorded from the Kwajalein station and P3 the third from Poker Flat. If more than one segment of data is used from a given pass, a second index indicating which record the segment begins in is assigned. For example, A4R16 starts in the sixteenth record of pass A4.

3.3 Analysis Procedures

Of initial importance when examining the data are several second order statistics: scintillation index and phase standard deviation. The data

is plotted to locate periods of scintillation and these statistics are used to verify it emperically and evaluate its stationarity. Their dependence on frequency is also of interest.

The scintillation index, S_4, is defined as the normalized standard deviation of the intensity.

$$S_4^2 = \frac{<I^2>-<I>^2}{<I>^2} \qquad (3.3.1)$$

Likewise, phase scintillation is displayed by the standard deviation.

$$\sigma_\phi = \sqrt{<\phi^2>-<\phi>^2} \qquad (3.3.2)$$

These are computed, for discrete data points, using the standard arithmetic mean formula.

$$<x> = \frac{1}{n} \sum_{k=1}^{n} x_k \quad , \text{ n values of x} \qquad (3.3.3)$$

After locating periods of scintillation, segments of stationary data must be isolated for further processing. Stationarity implies, ideally, that the above second order statistics remain time-invariant. For my purposes I established the criteria that the standard deviation of S_4 be less than 20% throughout the duration of the segment. After selecting stationary data segments, two types of correlation were computed; complex autocorrelation and real autocovariance. The complex autocorrelation requires that the data be in the form:

$$U = X+jY, \ X = A \cos\phi, \ Y = A \sin\phi \qquad (3.3.4)$$

The mean, $<U>$, is then computed as well as the autocorrelation

$$R_U(\tau) = <U(t)U*(t+\tau)> \qquad (3.3.5)$$

Also of interest is the real autocovariance. This is computed individually
for amplitude and phase. The mean is removed and the autocorrelation formula
applied.

$$R_A(\tau) = <(A(t)-<A>)(A(t+\tau)-<A>)>$$
$$= <A(t)A(t+\tau)>-<A>^2 \tag{3.3.6}$$

The real autocovariances and the logarithm of the complex autocorrelation are
then saved for spectral computations.

The computation of power spectra is facilitated by the fact that for a
given random variable, the autocovariance and power spectrum form a Fourier
transform pair. Thus, if a signal's autocovariance is known, the power spec-
trum can be realized by evaluating it in the frequency domain. The computational
situation is somewhat more complex so I will outline the details essential
for this realization. In an ideal case, the input data and the autocorrelation
would be continuous and extend from negative infinity to positive infinity in
time. In the practical situation, the data is sampled every τ_S seconds. The
data itself extends for τ_n seconds while its autocovariance lasts for time
τ_m. These limitations reduce the computations to a statistical estimation and
present several sources of error.

Initially, an error is introduced by the finite record length in the time
domain. Confidence limits for the spectral estimation must be evaluated
(Blackman & Tukey, 1958). For record length τ_n and autocovariance length
τ_m the degrees of freedom, k, can be established.

$$k = \frac{2\tau_n'}{\tau_m} , \quad \tau_n' = \tau_n - \frac{1}{3}\tau_m \tag{3.3.7}$$

The interval for 90% confidence can then be expressed

$$\text{interval} = \frac{20}{\sqrt{k-1}} \quad dB \quad , \quad k \geq 4 \tag{3.3.8}$$

Another important result of a finite time domain record is that the spectrum is window distorted. The definite start and stop of data is actually multiplication by a rectangular window (Oppenheim and Schafer, 1975).

$$W_R(t) = \begin{cases} 1 & 0 \le t \le \tau_m \\ 0 & t < 0, t > \tau_m \end{cases}$$
(3.3.9)

In the frequency domain, this convolves a spectrum of the form sin x/x with the desired spectrum.

The large sidelobes of the sin x/x function contribute significantly to distortion of the spectrum being analyzed. Hence, it is essential that the time domain data be multiplied by a window with smaller sidelobes prior to transformation. Ideally, the window's spectrum would be an impulse at DC. For practical purposes, the Hanning window provides a good compromise.

$$W_H(t) = \begin{cases} 0.5 + 0.5\cos(\frac{\pi t}{\tau_m}) & 0 \le t \le \tau_m \\ 0 & t < 0, t > \tau_m \end{cases}$$
(3.3.10)

Even with small sidelobes, any DC spectral component will display them as distortion in the final computation. For this reason, it is essential that the mean be removed from the time domain data at some point in the processing.

The range of frequencies to be observed in the power spectra arises as a point of interest. The sampling theorem indicates that data in discrete-time are reliable only for frequencies below $(2\tau_s)^{-1}$, where τ_s is the sampling period (Lathi, 1974). In this case, $\tau_s = 0.01$ seconds so 50 Hz is the highest useful frequency.

At the low end of the scale, the point at which the data becomes useful is determined by the frequency resolution, Δf_r. Any variations in an interval

from 0 Hz to Δf_r are too slow to be resolved. For this reason, meaningful spectral information is available only past this interval. This resolution is given by (Lovelace et al., 1970).

$$\Delta f_r = 1/\tau_m \tag{3.3.11}$$

So to yield two decades of useful spectrum

$$\Delta f_r = 0.5 \text{ Hz}$$
$$\tau_m = 2 \text{ seconds} \tag{3.3.12}$$

While greater resolution could be obtained, it would decrease the confidence, as indicated above.

In order to keep the spectrum "smooth" the discontinuity at time zero must be removed. This sudden step would obviously introduce high frequency components. To do this, the data is replicated in reverse order at the end of the record.

The total length of the time series record must be a power of two in order to implement the fast Fourier transform algorithm. In order to "stretch" the data to the appropriate length, zeroes are appended to the end of the windowed autocovariance. The resultant record input to the transform is of the form shown in Fig. 3.3.1.

The effects of this also include the addition of a neater appearance to the spectral plot. Because the spectra can be evaluated only at discrete frequencies the spacing of these frequencies becomes important. Too great a distance adds uncertainty to the space between frequencies or the picket fence effect (Oppenheim & Schafer, 1975). The frequency increment is given by

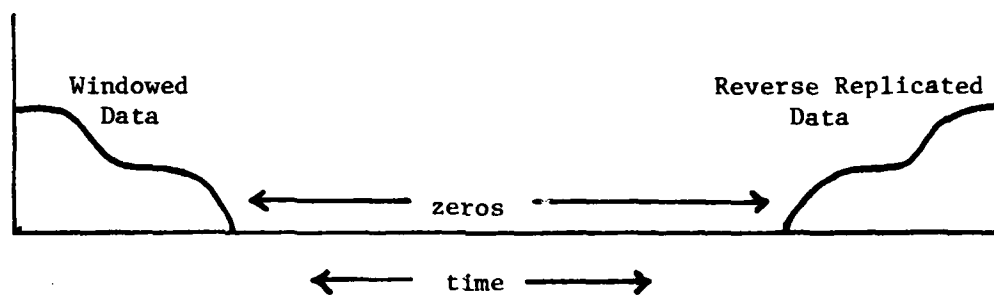$$\Delta f_S = \frac{1}{N\tau_S} \text{ Hz} \tag{3.3.13}$$

Fig. 3.3.1 Form of Data Input to Transform

where N is the number of points in the transform. $N=2^{11}=2048$ points proves to yield good results.

Thus, a typical spectral computation will procede as follows. τ_n seconds of data are reduced to τ_m seconds of autocovariance by subtracting the mean and autocorrelating. The result is then multiplied by the Hanning window and input, along with its mirror image and zeroes, to the FFT. The result is a spectral estimation with:

(1) 90% confidence within $\dfrac{20}{\sqrt{k-1}}$ dB

(2) a useful range from 0.5 Hz to 50 Hz and resolution of 0.5 Hz

(3) values computed every $\dfrac{1}{(0.01)(2048)} = 0.049$ Hz

Plots are generated of the detrended data, amplitude and phase scintillation statistics, autocorrelation and spectra.

As related in Chapter 2, a power law behavior is expected in the spectra. At the high frequency end this translates to a linear relationship between the logarithm of the magnitude (dB level) and the logarithm of the frequency. Thus, as part of the plotting process, I have fit lines to the curves.

A standard software package is employed that utilizes the least-squares method for linear regression. The plot is first inspected to determine the upper and lower frequencies between which the line is drawn. The lower frequency is at the corner defined by either the spectral resolution, detrend frequency, or Fresnel frequency in the case of weak amplitude scintillation. The upper frequency is that at which noise becomes dominant.

4.   Experimental Results

4.1 Pass Characterization

After examination of the time variation of second-order statistics of the data, several relatively stationary data segments were selected from each receiving station. The plots of one such segment, ten second detrended, are available in Appendix 1. Preliminary analysis shows some general attributes of different geographic locations of reception.

Scintillation strength varies greatly at different latitudes. The equatorial stations recorded the most acitivity with the Ancon data being the stronger of the two. The auroral station showed much weaker amplitude scintillation but had phase fluctuations on the same order. The data taken at mid-latitude, however, showed very little activity.

At any latitude, scintillation level varies with frequency. The scintillation index is employed as an indication of the level of amplitude fluctuation. Recall 3.3.1

$$S_4^2 = \frac{<I^2> - <I>^2}{<I>^2} \tag{4.1.1}$$

Averaged values of S_4 are plotted for each receiving station in Fig. 4.1.1.

Some type of f^{-n} variation is observed immediately. The Poker Flat case shows an almost constant-slope with $n \approx 1.29$. Examination of the Ancon and Kwajalein cases reveals that the slope is actually changing. In the limiting case it appears that at saturation ($S_4 \to 1$) the slope approaches zero. With very small S_4, however, $n \to 1.5$. The erradic behavior of the Stanford case is most likely attributable to a noise level on the same order as that of the scintillation.

In a similar manner, the frequency dependence of phase scintillations can be analyzed. The standard deviation (3.3.2) is used
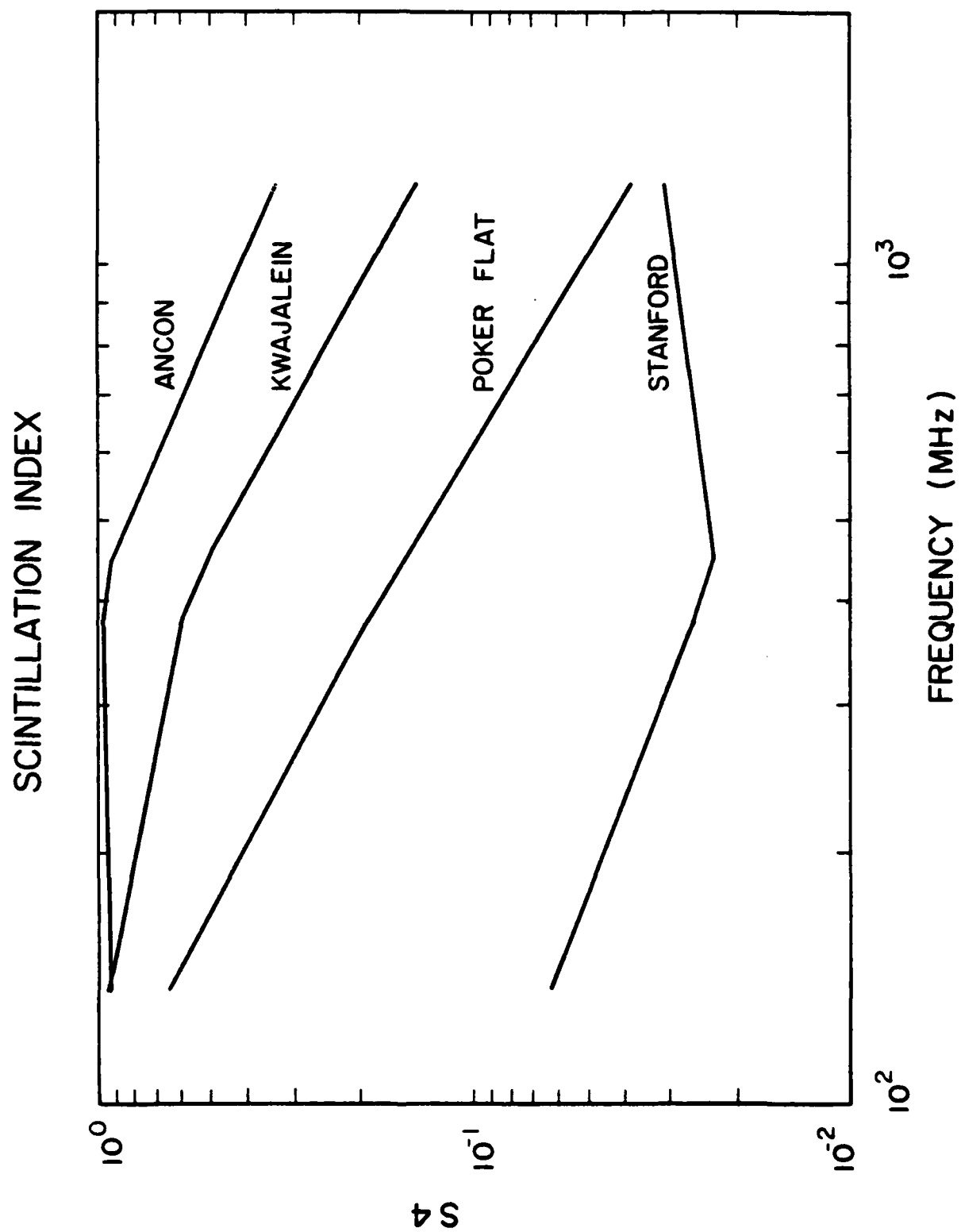
Fig. 4.1.1 Scintillation Index

$$\sigma_\phi = \sqrt{<\phi^2>-<\phi>^2} \qquad (4.1.2)$$

Again, averaged values for each station are plotted (Fig. 4.1.2).

In most cases, σ_ϕ varies as $1/f$. Again, however, some levelling off is apparent for very intense activity. For the Stanford data, phase scintillation is much higher than the noise level. This level is easily observed because the S-based phase, supposedly identically zero, has a standard deviation of a few thousandths.

4.2 The Average Field

The levels of electron density fluctuation can also be observed for various passes by noting the mean of the complex signal as in (3.3.4). Recall (2.3.5):

$$<U> = U_0 \exp[-\frac{k^2 L}{8} A(0)] \qquad (4.2.1)$$

This leads to

$$\ln<U>^2 = \ln\{U_0{}^2\exp[-\frac{k^2 L}{4} A(0)]\}$$
$$= 2\ln U_0 - \frac{k^2 L}{4} A(0) \qquad (4.2.2)$$

By observing from (2.3.1) and (2.3.3)

$$\Gamma_2 = <U(z,\vec{\rho}_1)U^*(z,\vec{\rho}_2)> = U_0{}^2\exp\{-\frac{k^2 z}{4} [A(0)-A(\vec{\rho})]\} \qquad (4.2.3)$$

and evaluating at $\vec{\rho}=0$

$$\Gamma_2 \bigg|_0 = <U^*U> = U_0{}^2 \qquad (4.2.4)$$

Recalling that $<U^*U>\cong 1$ rewrite (4.2.2) as
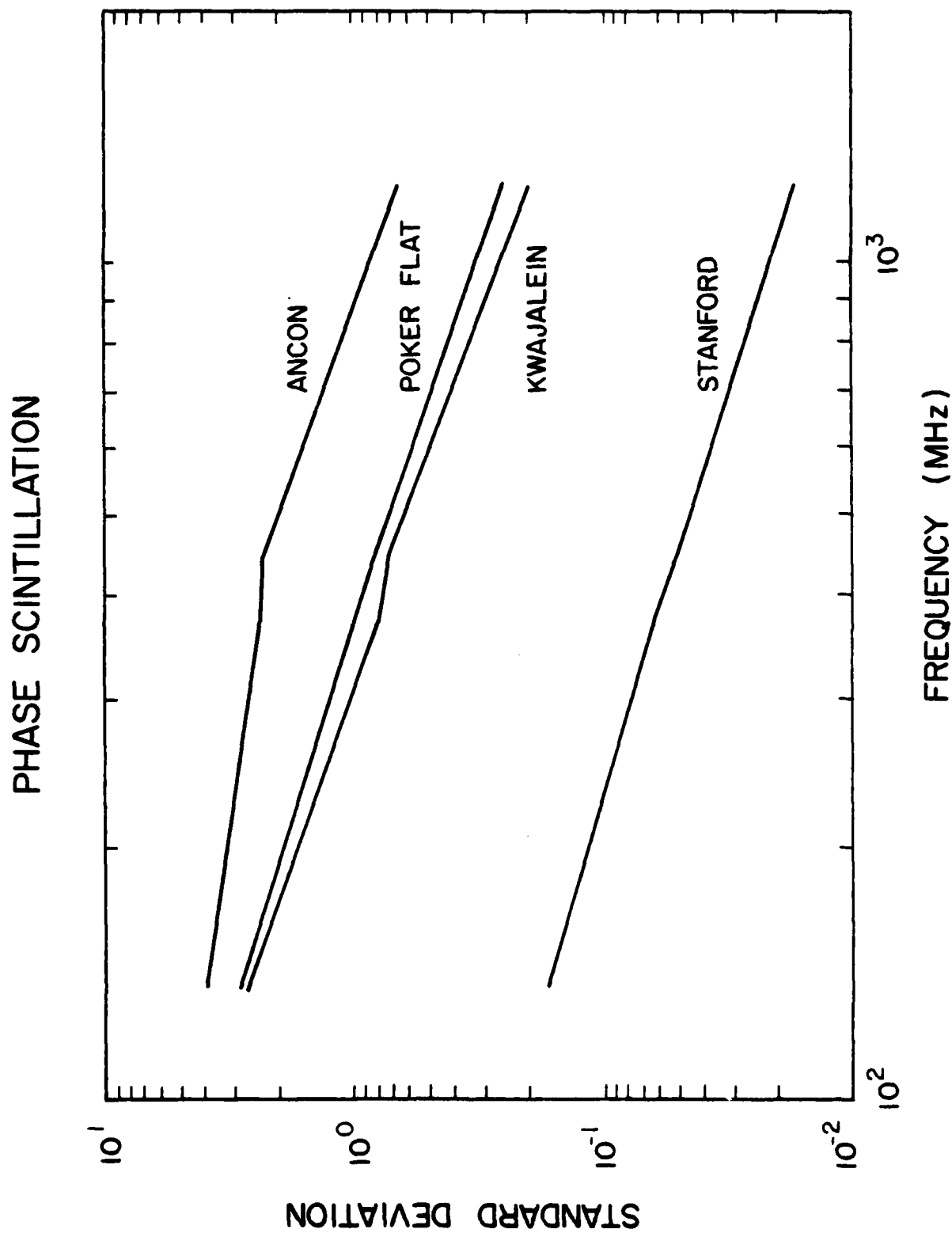
Fig. 4.1.2 Phase Scintillation

$$\ell n<U>^2 = - \frac{k^2 L}{4} A(0) \qquad (4.2.5)$$

from the results of (2.3.7) and (2.3.8) this can be rewritten as

$$\ell n<U>^2 = - \frac{\pi^2 f_{p0}^4 L}{c^2 f^2} A_N(0) \qquad (4.2.6)$$

Thus, the correlation function of the electron density fluctuation, A_N, is available.

For a given value of $A_N(0)$ equation (4.2.6) implies that

$$\ell n<U>^2 \propto \frac{1}{f^2} \qquad (4.2.7)$$

or

$$\frac{\ell n<U_1>^2}{\ell n<U_2>^2} = (\frac{f_2}{f_1})^2 \qquad (4.2.8)$$

This hypothesis was tested with several sets of data. Some of the characteristics of these data sets are given in Table 4.2.1.

TABLE 4.2.1 Mean Fields and Scintillation Indices

Pass	Frequency (MHz)	S_4	$<U>$	$\ell n<U>^2$
K2R4	378	0.655	.598-.081j	-1.0283
	447	0.605	.772-.025j	-0.6794
	1239	0.163	.969-.011j	-0.063
K4	378	0.549	.699-.044j	-0.7162
	447	0.416	.770-.042j	-0.5227
	1239	0.121	.974-.007j	-0.05269
P3	378	0.068	.862-.013j	-0.297
	447	0.057	.899-.008j	-0.213
	1239	0.018	.990-.002j	-0.0201
P3R16	378	0.289	.503-.08j	-1.3743
	447	0.228	.621-.065j	-0.9528
	1239	0.055	.96-.017j	-0.0816

For each case equation 4.2.8 is applied yielding the results in Table 4.2.2.

TABLE 4.2.2   Ratios from equation 4.2.8

Pass	$\left(\dfrac{\ell n{<U_{378}>}^2}{\ell n{<U_{447}>}^2}\right)$	$\left(\dfrac{\ell n{<U_{447}>}^2}{\ell n{<U_{1239}>}^2}\right)$
K2R4	1.51	10.78
K4	1.37	9.92
P3	1.39	10.60
P3R16	1.44	11.67
expected	1.40	7.68

For the low frequency case an average error of about 3.5%   is observed.   In the case of the higher frequency, however, about 40% error occurs.   This error is probably attributable to the fact that <U> is so close to unity in the L-band its logarithm is very close to zero.   This makes the calculations highly sensitive to even a small error.

The next step is to isolate the frequency independent information from these data.   Rewrite 4.2.6 as

$$A_N(0) f_{p_0}{}^4 L = - \frac{f^2 c^2}{\pi^2} \, \ell n {<U>}^2 \qquad (4.2.9)$$

Now, for a given pass, $A_N(0) f_{p_0}{}^4 L$ should be constant.   Examine table 4.1.3.

Especially for the upper two frequencies, the computed values remain very close.   In addition comparing the computed value for each pass with the level of scintillation indicated in Table 4.1.1 shows another trend.   As is to be expected.   The amount of scintillation varies with the amount of electron density fluctuation.

TABLE 4.2.3. Density fluctuation coefficient

pass	frequency (MHz)	$A_N(0)f_{p_0}{}^4L$
K2R4	378	1.34×10^{33}
	447	1.238×10^{33}
	1239	8.819×10^{32}
	mean	1.153×10^{33}
K4	378	9.33×10^{32}
	447	9.52×10^{32}
	1239	7.38×10^{32}
	mean	8.74×10^{32}
P3	378	3.87×10^{32}
	447	3.88×10^{32}
	1239	2.8×10^{32}
	mean	3.52×10^{32}
P3R16	378	1.79×10^{33}
	447	1.74×10^{33}
	1239	1.14×10^{33}
	mean	1.56×10^{33}

4.3 Correlation Characteristics

The autocorrelation of the complex signal is displayed in Fig. 4.3.1 for pass K4 at VHF. It is important to note that, ideally, the autocorrelation is purely real. Comparison of the magnitudes of the real and imaginary parts helps to indicate how "good" the data is.

Because, as related earlier, <U*U> is set at unity in the field the following result is implied.

$$\ln \Gamma_2 \big|_{t=0} = \ln <U*U> \equiv 0 \qquad (4.3.1)$$

This prevents calculations like the ones carried out for the average field.

Seperate correlations for amplitude and phase raise some interesting points, though. Define the correlation interval τ to be the time it takes for the autocovariance to drop to one half. Thus, smaller τ corresponds to quicker decorrelation.

For amplitude, a dependence of τ_A on frequency and S_4 is noted. The various passes were separated into three groups based on S_4 in the L-band. At each frequency, within each group, the mean τ_A is evaluated. The results are plotted in Fig. 4.3.2. For each group the values are normalized with respect to the L-band value.

The best behaved curve, that of group 3, is very nearly proportional to $f^{-1/2}$. This is attributable to the Fresnel filtering effect related in Chapter 2. For weak scintillation this inverse square relation is to be expected (Umeki, et al., 1977a).

For the more intense cases, however, a marked decorrelation at low frequencies occurs. The exact behavior is difficult to assess because of the gap between 447 MHz and 1239 MHz. In both cases it seems that τ_A
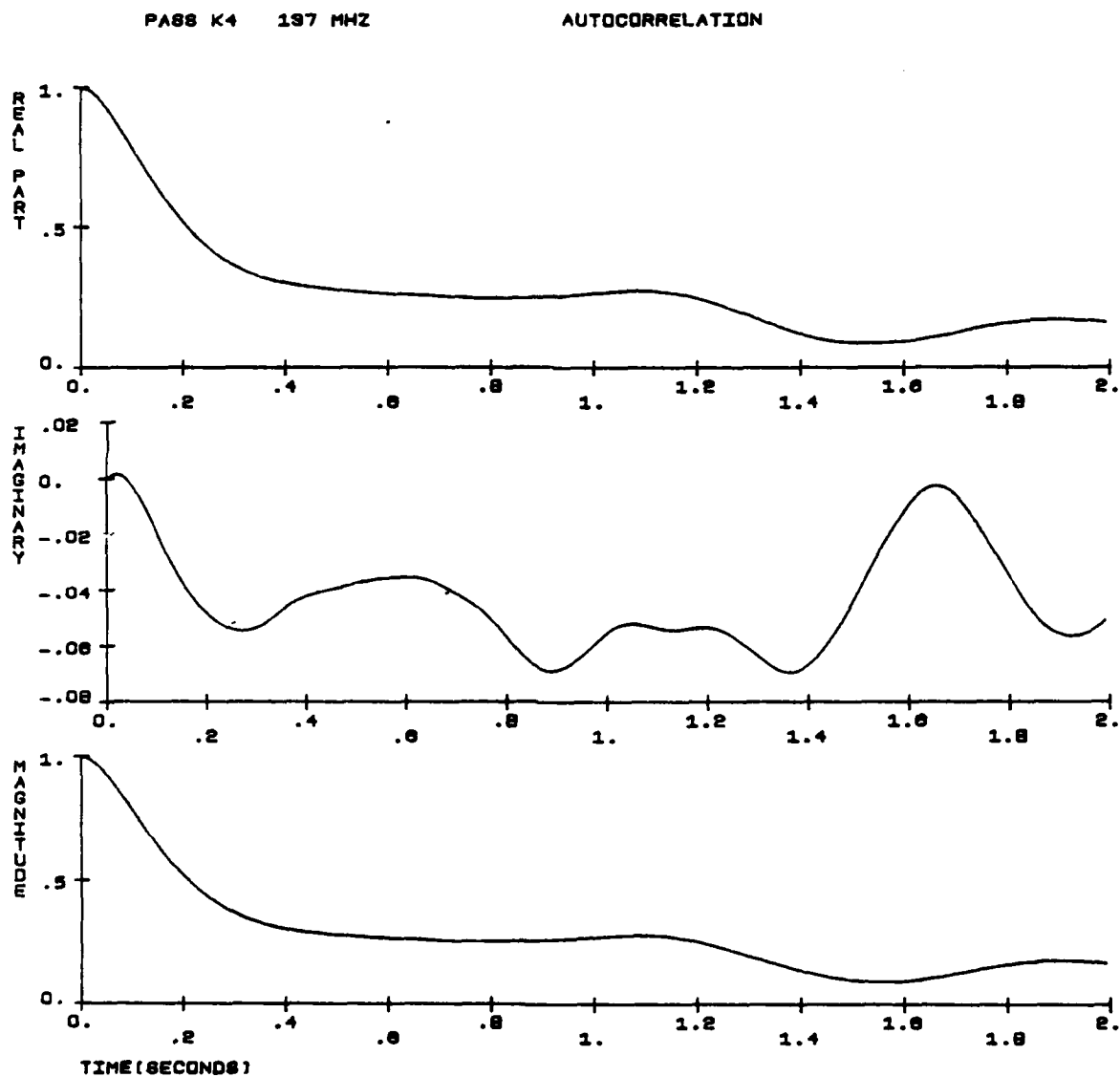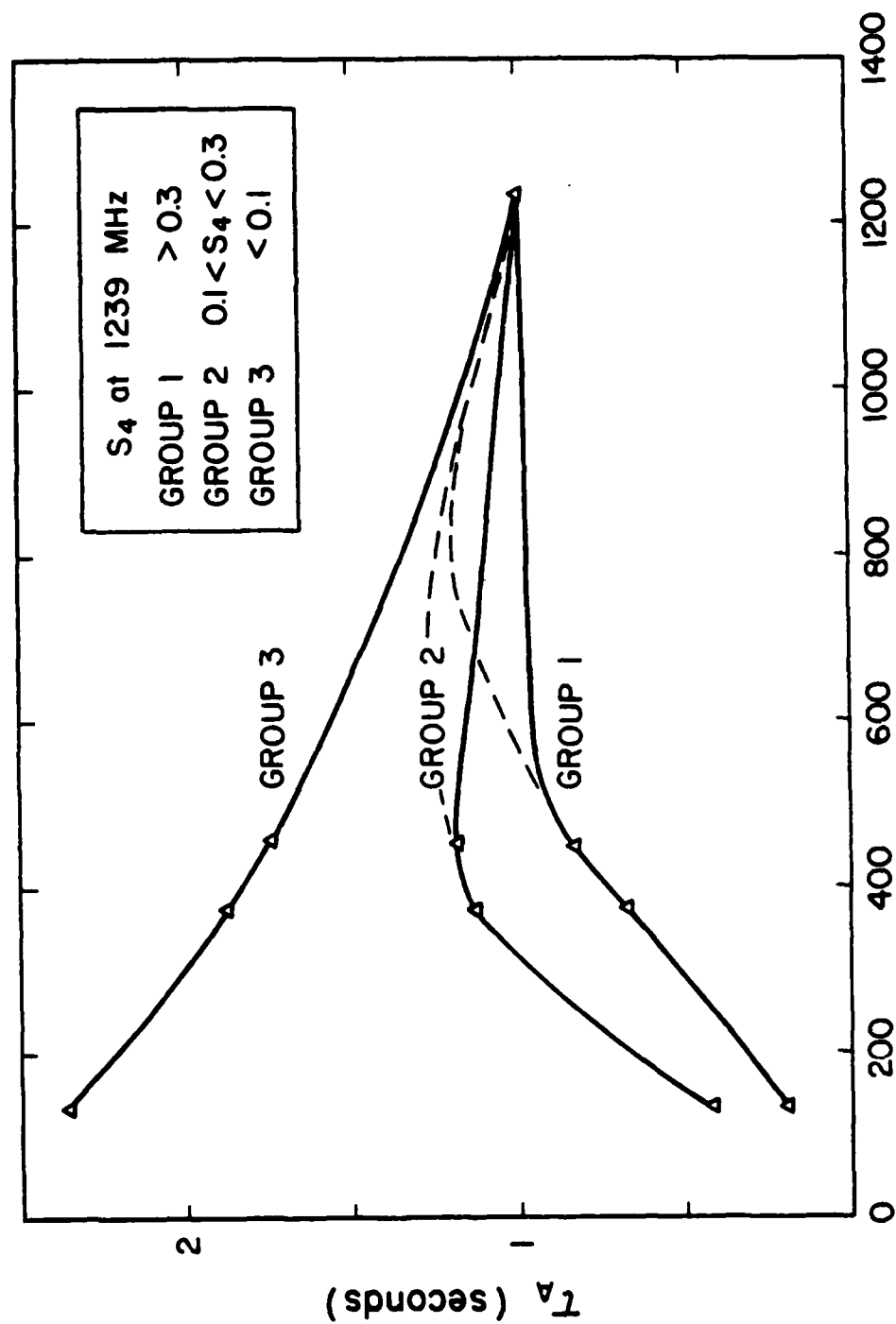
Fig. 4.3.1 Pass K4 VHF Autocorrelation

Fig. 4.3.2 Amplitude Decorrelation

increases with frequency up to some point in the UHF band and then decays slightly into the L-band.

A useful task might be to determine the S_4 value under strong scintillation conditions for which a signal is best correlated. A reasonable hypothesis seems to be that maximum correlation occurs for signals with $S_4 \approx 0.7$. For group two this occurs around 447 MHz and for group one between 447 MHz and 1.2 GHz.

The frequency dependence of phase autocovariance is an entirely different situation. The mean correlation interval $<\tau_\phi>$, is plotted in Fig. 4.3.3 for each of the three groups. The Fresnel filtering is absent from phase scintillation. Thus, in the weak case of group 3, the correlation interval is almost frequency independent. Multiple scattering is evident in the stronger groups, however, inducing increased decorrelation at the low frequency end of the scale.

4.4 Power Spectra

Three types of spectra are available at each frequency for each data set. These are the power spectra of amplitude, phase and $L=\ln\Gamma_2$. These are notated as P_A, P_ϕ, and P_L. The various spectra will be presented in three ways. First, those for an individual data set from each receiving station will be discussed. Next, different segments from the same pass will be examined. Finally, several spectra will be compared in order to note any geographic trends.

Amplitude spectra from pass K4 are presented in Fig. 4.4.1. The primary difference between the VHF and UHF channels involves the corner frequency around 1 Hz. Notice the broadening in the VHF spectrum as opposed to the well defined corner at UHF. It can also be noted that the broader spectrum is associated with the higher scintillation index.

According to the results in Chapter 2 the phase spectrum should display the same asymptotic slope as its amplitude counterpart. Fig. 4.4.2 does not
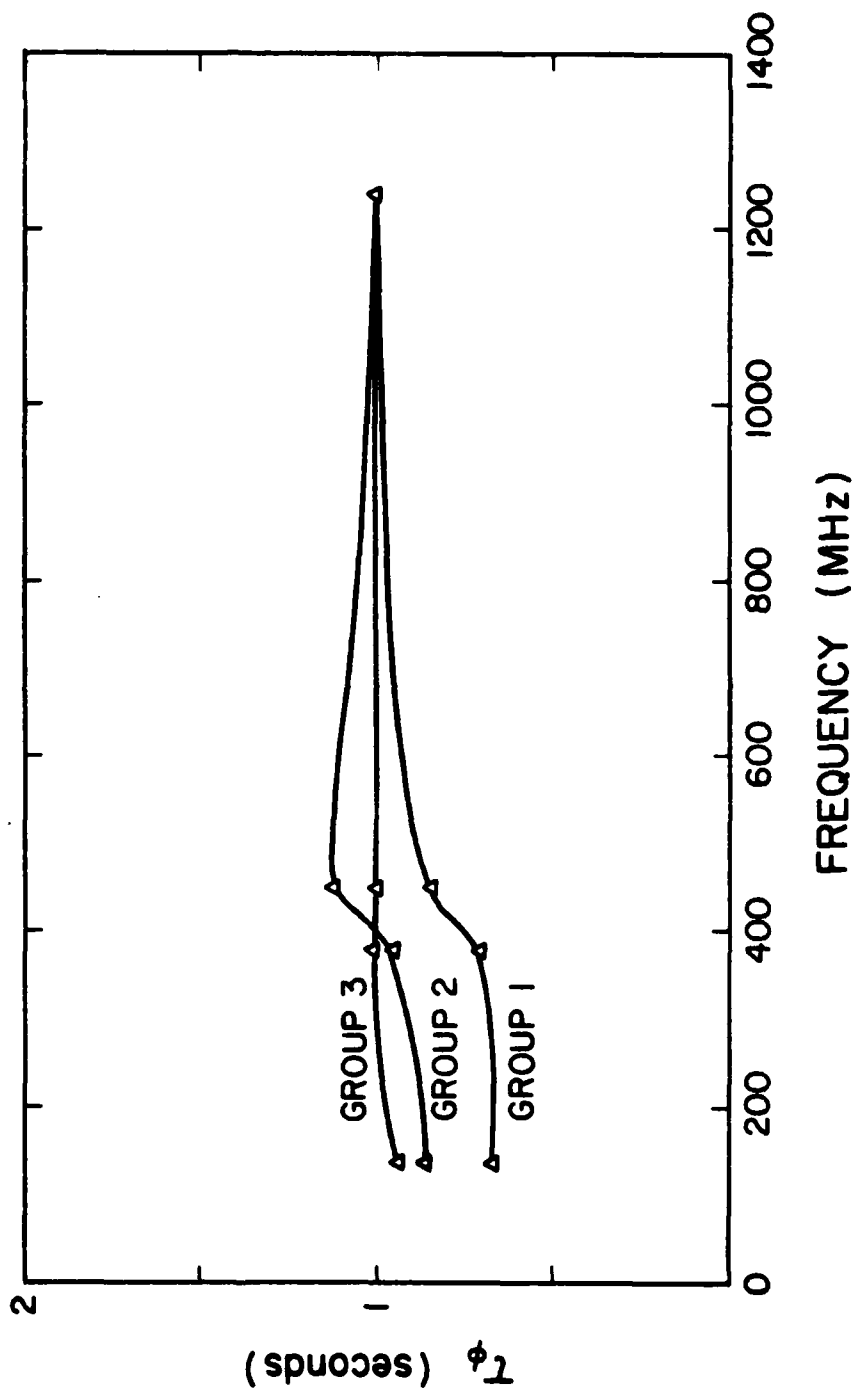
NORMALIZED PHASE
CORRELATION INTERVAL

GROUP 3
GROUP 2
GROUP I

τ_ϕ (seconds)

FREQUENCY (MHz)

Fig. 4.3.3 Phase Decorrelation
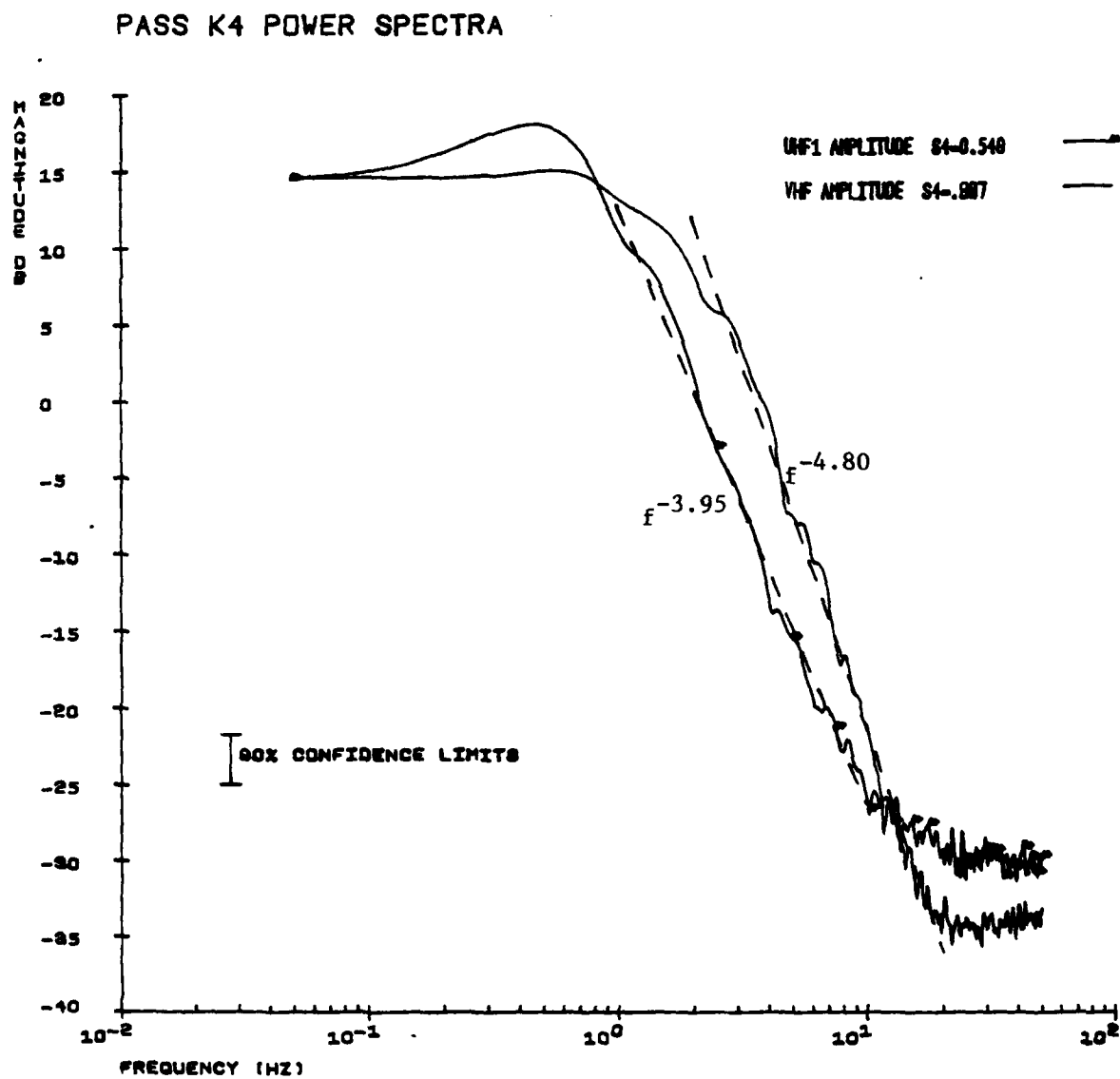
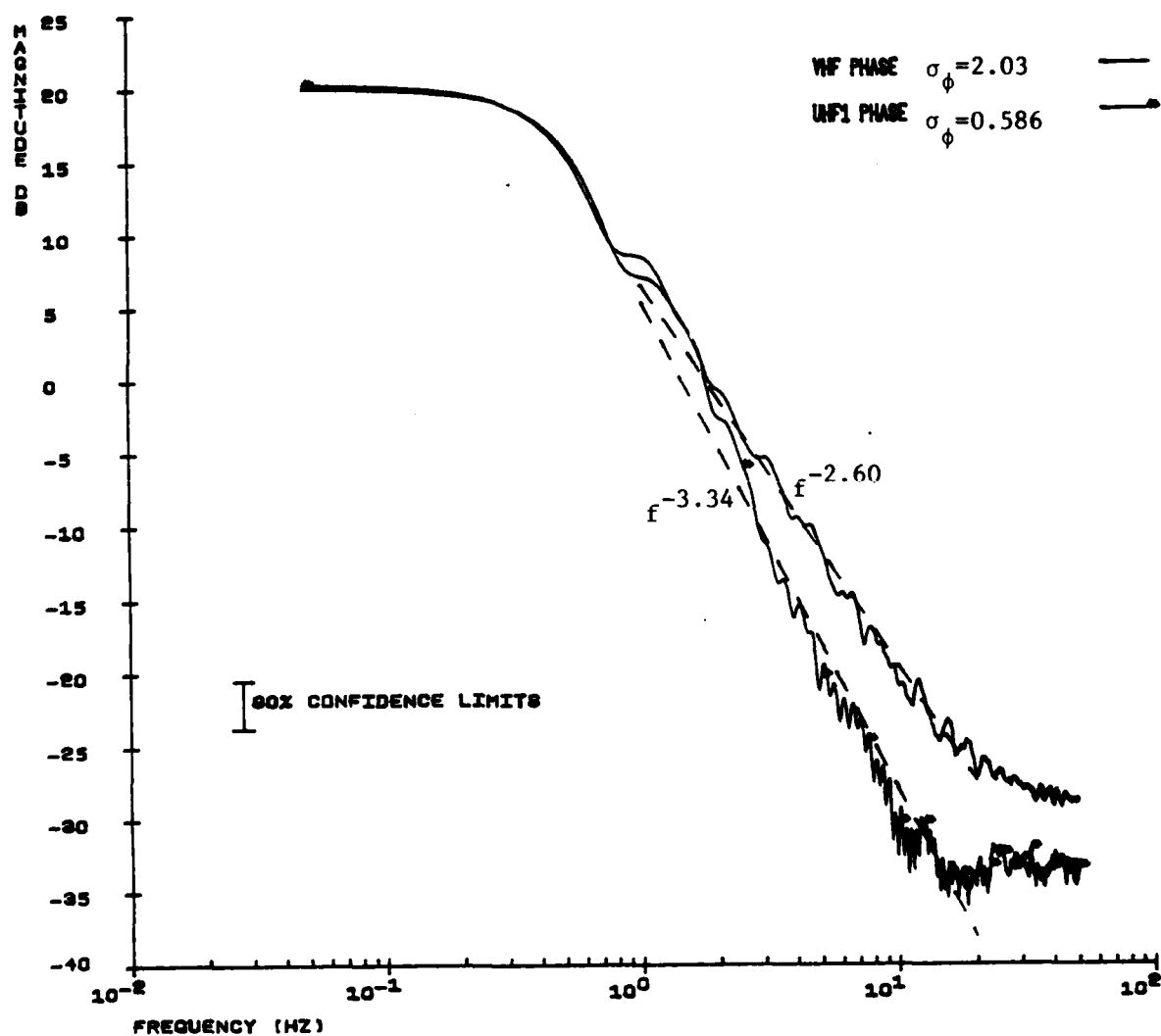Fig. 4.4.1 Pass K4 Amplitude Spectra
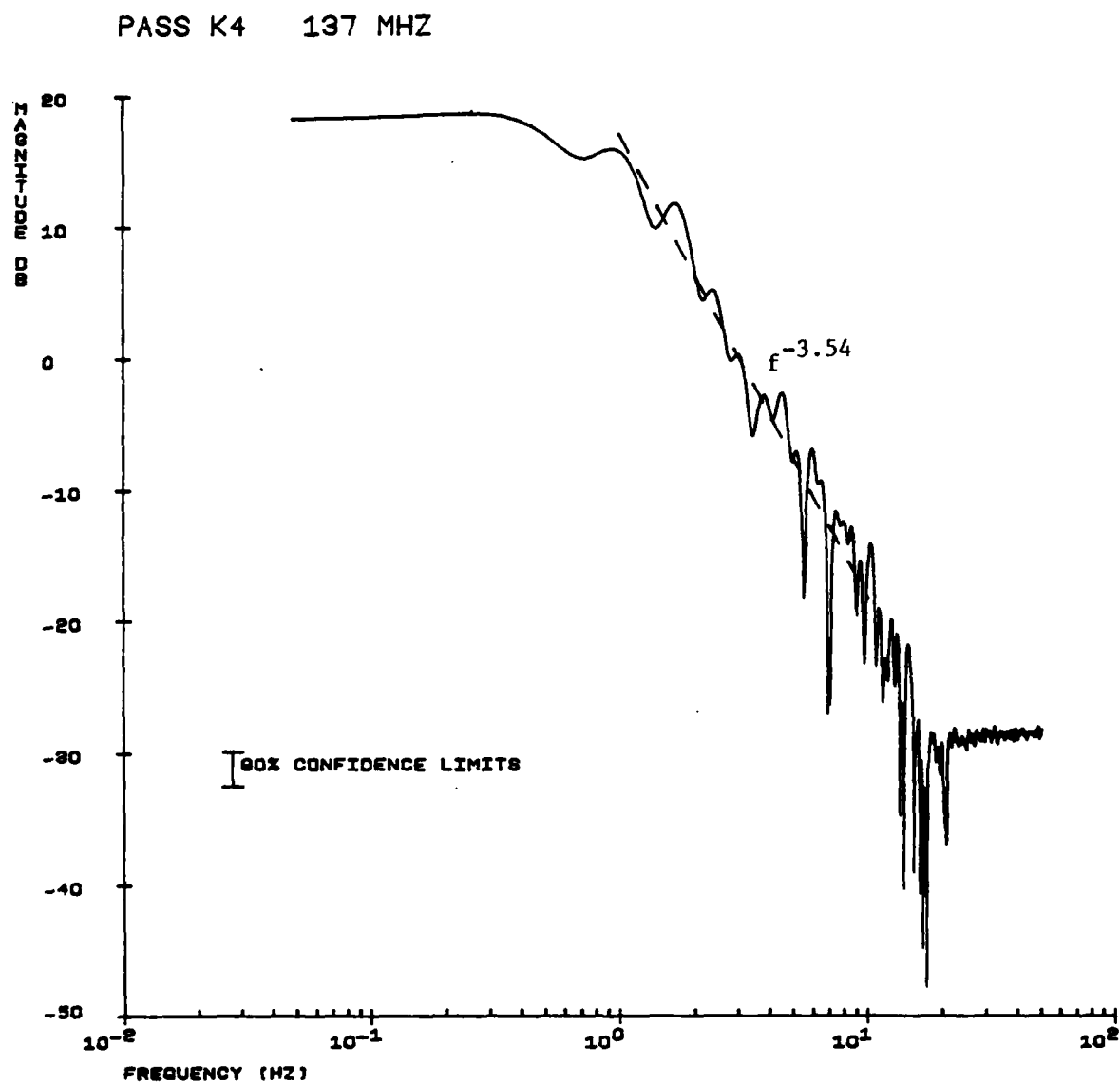
Fig. 4.4.2 Pass K4 Phase Spectra

bear this out when compared to the previous plots. With scintillation level approaching saturation, the VHF phase spectrum becomes flatter. At UHF, however, the amplitude and phase slopes are much closer.

Figures 4.4.3 and 4.4.4 show the P_L spectra at VHF and UHF. As predicted in theory, the two are very similar with the exception of more noise at VHF. This extra noise can be attributed to the fact that the imaginary part of the autocorrelation is slightly greater at VHF. Nonetheless, comparison with the UHF phase spectrum demonstrates a great deal of similarity. Therefore, where the phase spectrum is not flattened by very intense scintillation it coincides well with the power spectrum of the electron density fluctuations.

The amplitude spectra for pass A4R13 are shown in Fig. 4.4.5. Again, the VHF spectrum appears broader. Note, though, that the curve actually turns up to define a corner frequency whereas the UHF case, corresponding to a higher S_4, has a more obscure corner. In the L-band, the sharpest corner corresponds to the weakest scintillation. Differences in the leveling off at the right end of the spectra are due to differences in the relative level of quantization noise in the data.

A dominant characteristic of the phase spectra (Fig. 4.4.6) is some type of ringing. This is most evident in the L-band. As in the Kwajalein case strong scintillation corresponds to a flatter spectrum for phase than for amplitude. In this case it is true for both VHF and UHF.

The spectra from pass P3R16 confirm the same trends. The amplitude spectra (Fig. 4.4.7) show the same broadening for more intense scintillation. While noise causes the L-band slope to decrease rapidly, the corner frequency becomes more clearly defined as scintillation becomes weaker. Also of interest is the fact that the VHF and UHF asymptotes have approximately the same slope.

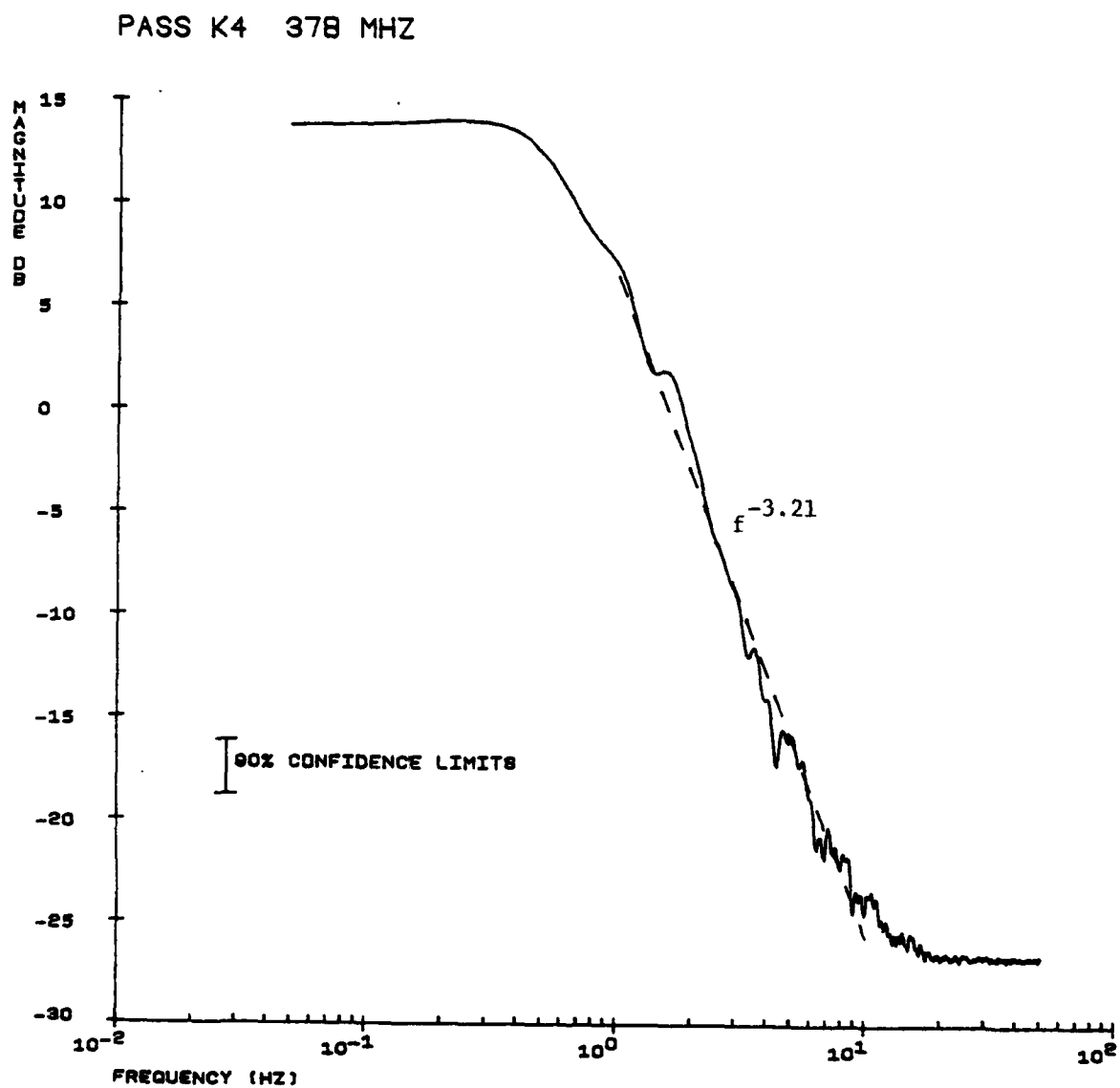Fig. 4.4.3 Pass K4 VHF P_L Spectrum

PASS K4   378 MHZ

Fig. 4.4.4 Pass K4 UHF P_L Spectrum
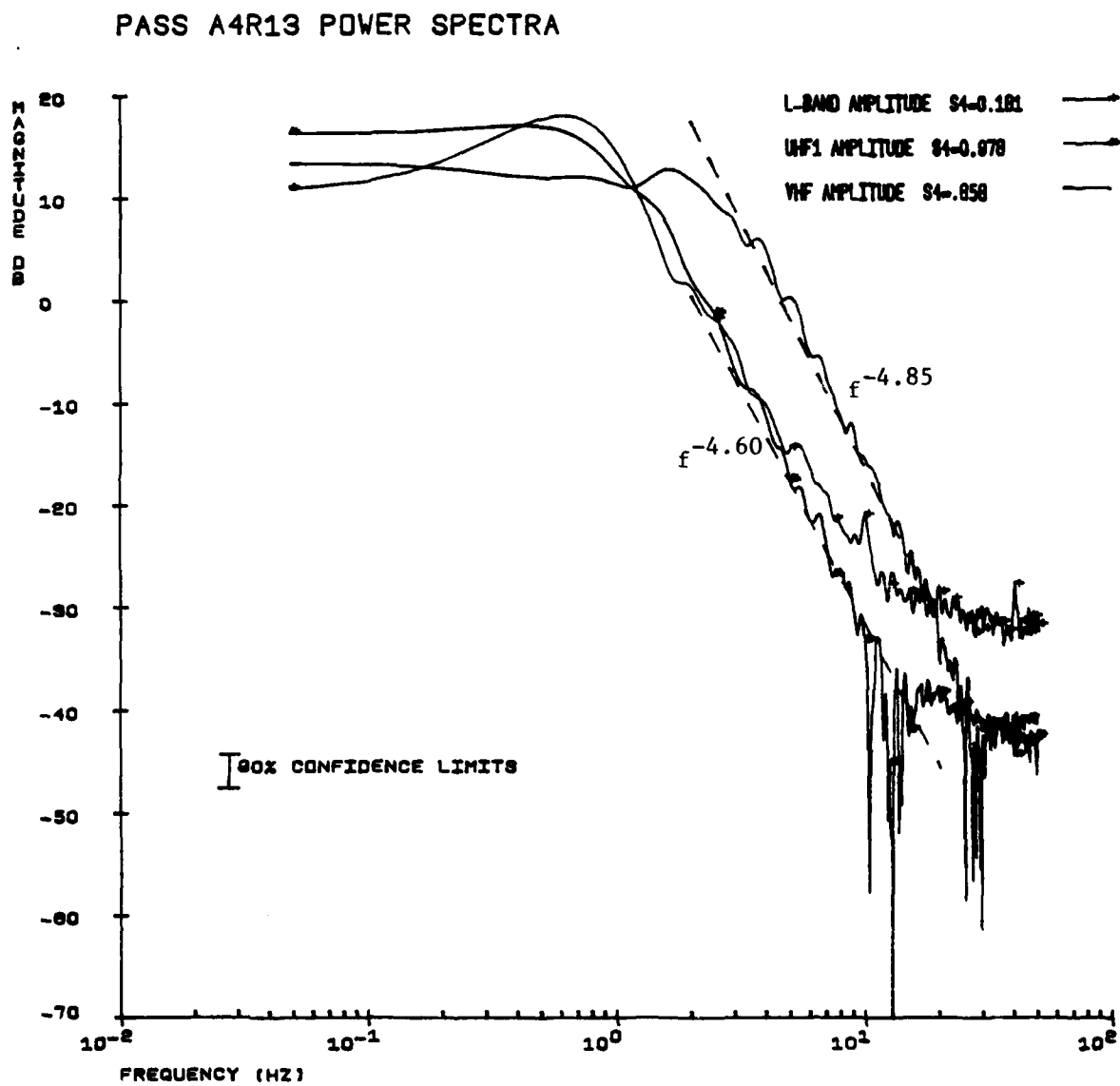
PASS A4R13 POWER SPECTRA

Fig. 4.4.5 Pass A4R13 Amplitude Spectra

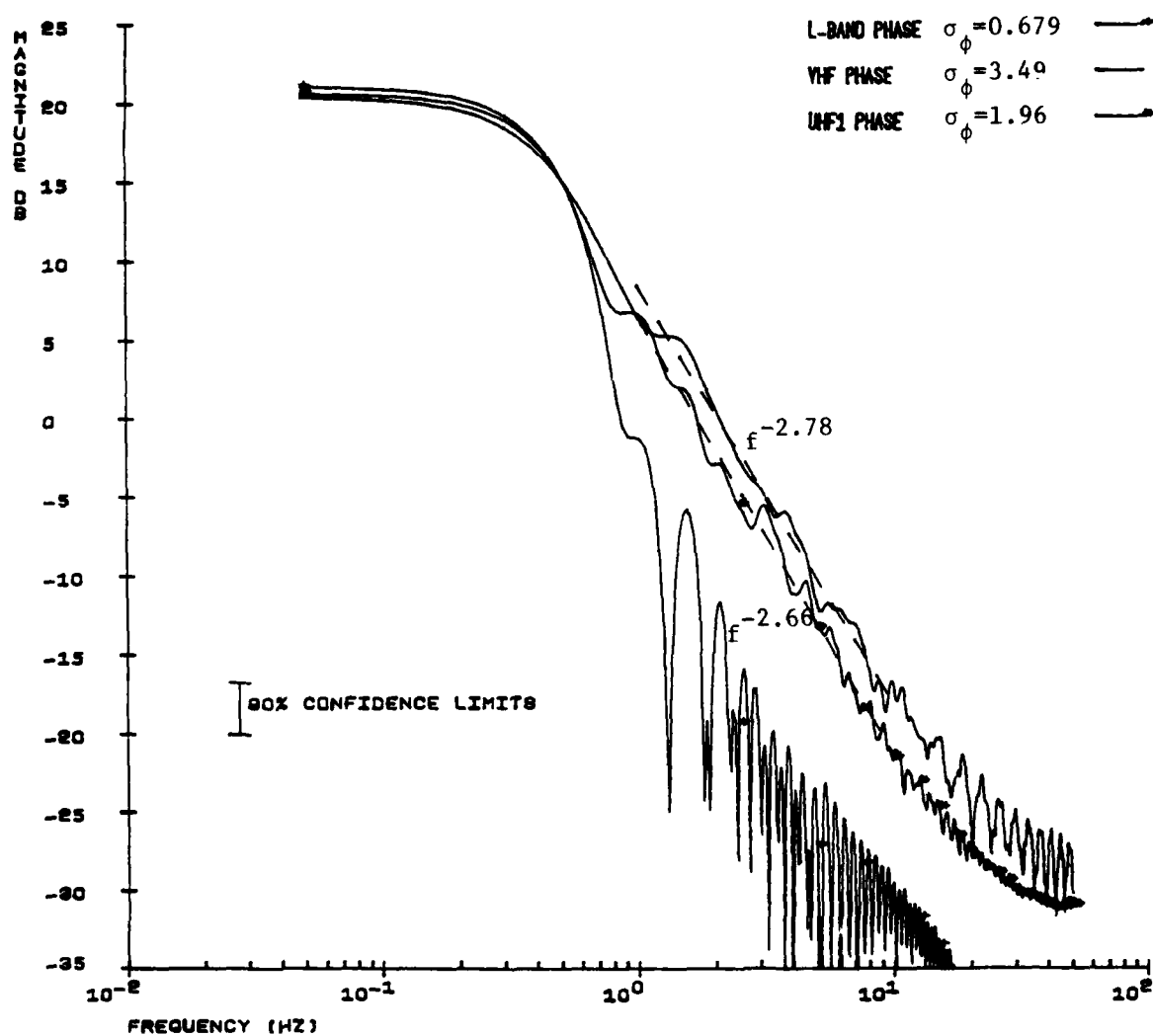## PASS A4R13 POWER SPECTRA

Fig. 4.4.6 Pass A4R13 Phase Spectra
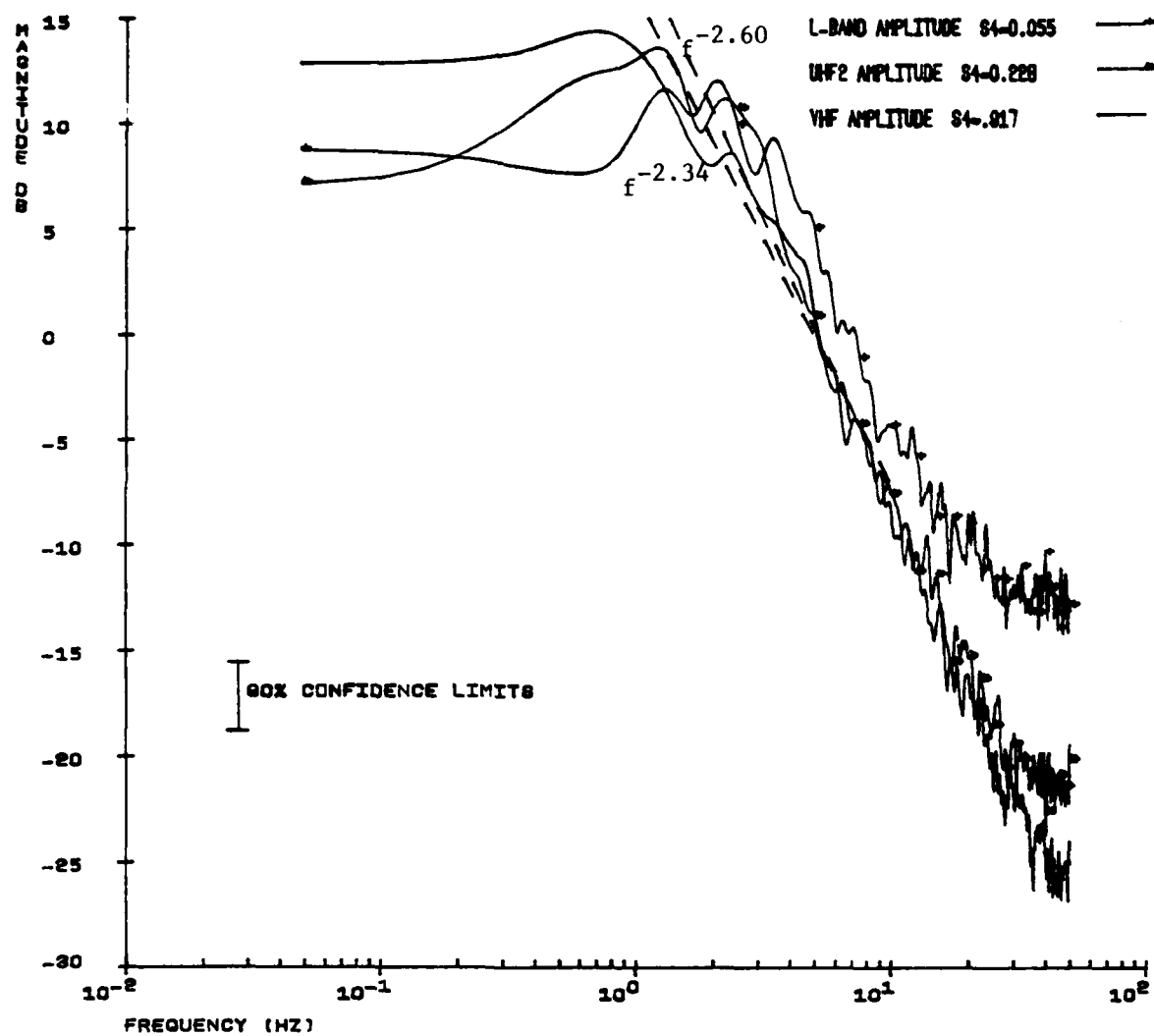
PASS P3R16 POWER SPECTRA

Fig. 4.4.7   Pass P3R16 Amplitude Spectra

The phase spectra (Fig. 4.4.8) behave per expectation. The VHF spectrum, a strong multiple scatter case, is somewhat flatter than the others. At UHF the slope is in the same range as that of the UHF amplitude spectrum. A confidence interval of about 3 dB can help explain some of the error.

VHF spectra for pass S1R5 show some difficulties typical of the mid-latitude data (Fig. 4.3.9). Noise, uncertainty and even some interference around 15 Hz are prominent. Notice, though, the very sharp corner in the amplitude spectrum. Based on earlier observations, this is appropriate for such a weak case. As predicted for weak scintillation, the amplitude and phase slopes are about the same.

One of the advantages of low level activity is that the data yields a very nearly real autocorrelation. The P_L spectrum for VHF is displayed in Fig. 4.4.10. Note the strong similarity to the phase spectrum. The curve drops off right at the half Herz resolution point with about the same slope. Some of the small scale detail, including the interference, is about the same.

Comparison of computations for different segments from the same satellite pass strengthens some of the previous conclusions. Spectra from pass P3 are shown in Fig. 4.4.11. Compare the VHF amplitude spectrum to that of P3R16 (Fig. 4.4.7). The slopes are about the same but in the weak case, P3, the corner frequency is more clearly defined. On the other hand, the phase spectra are about the same.

VHF spectra for pass A4R16 (Fig. 4.4.12) show similar behavior for an equatorial pass. From the same pass, the A4R13 VHF amplitude spectrum (Fig. 4.4.5) is not as broad. Correspondingly, the scintillation is not as strong in this case. The computed slopes are not the same but this is because the curves are not linear for the same range of frequencies. Again, for phase (Fig. 4.4.6) the spectra are about the same.
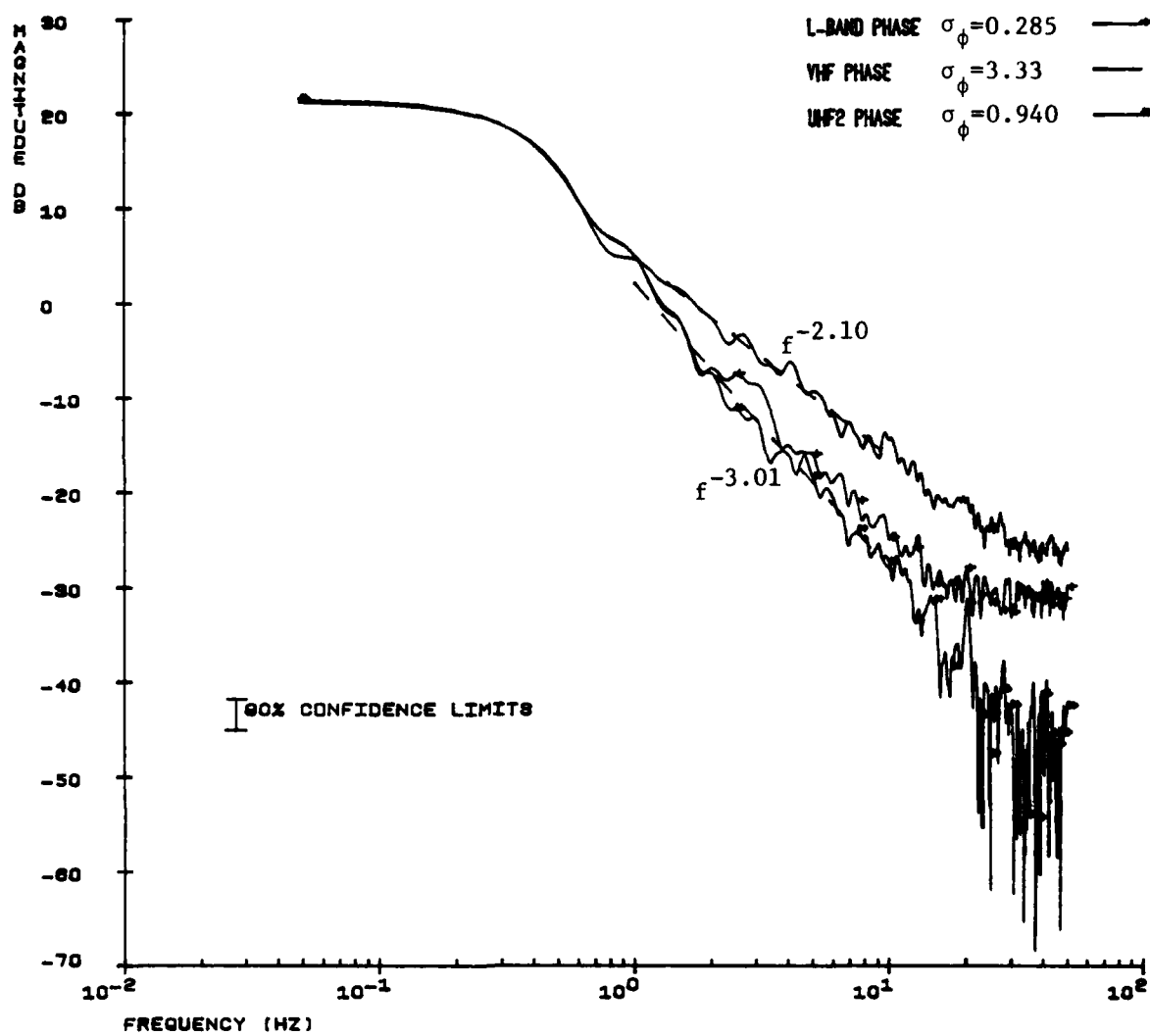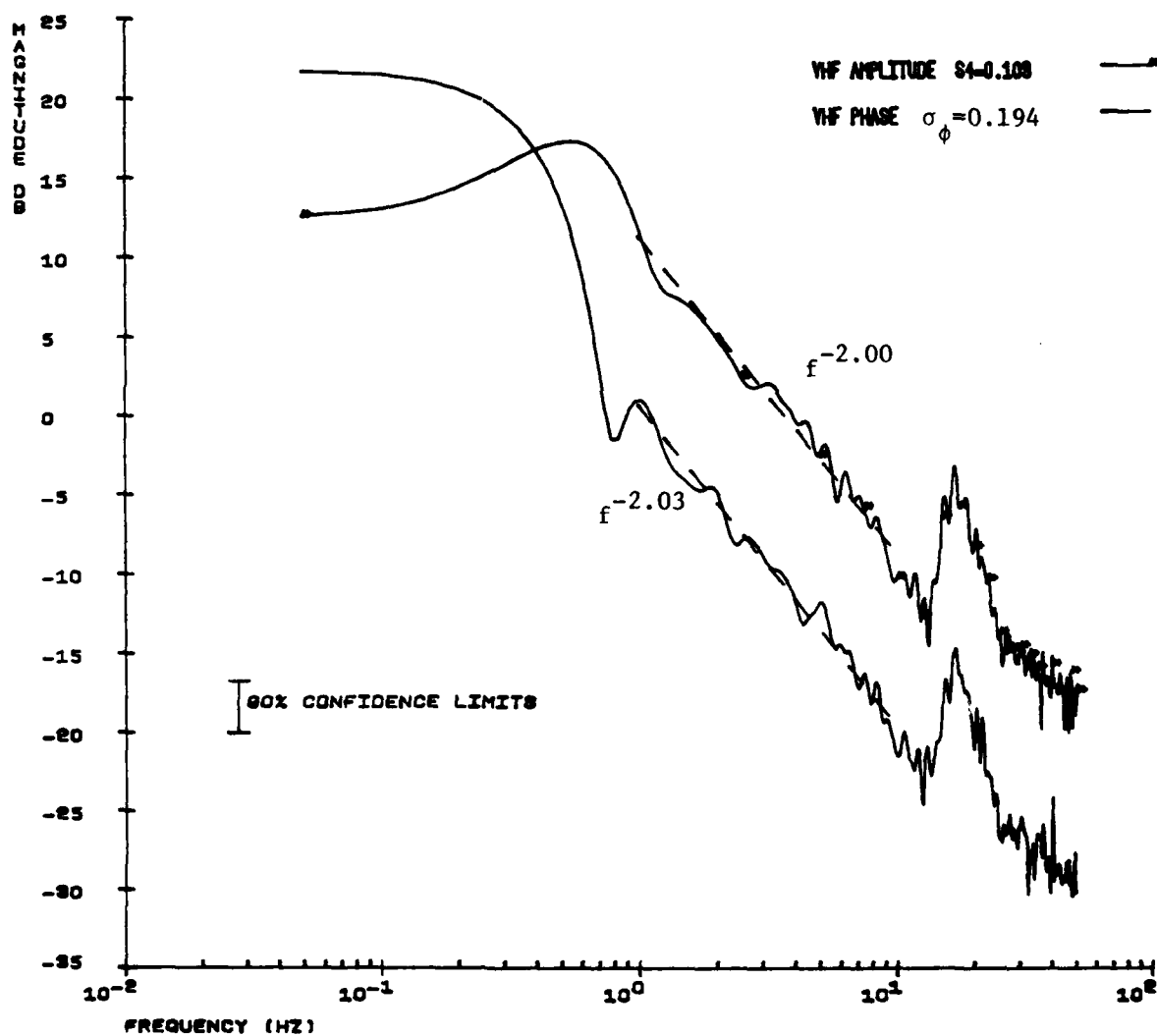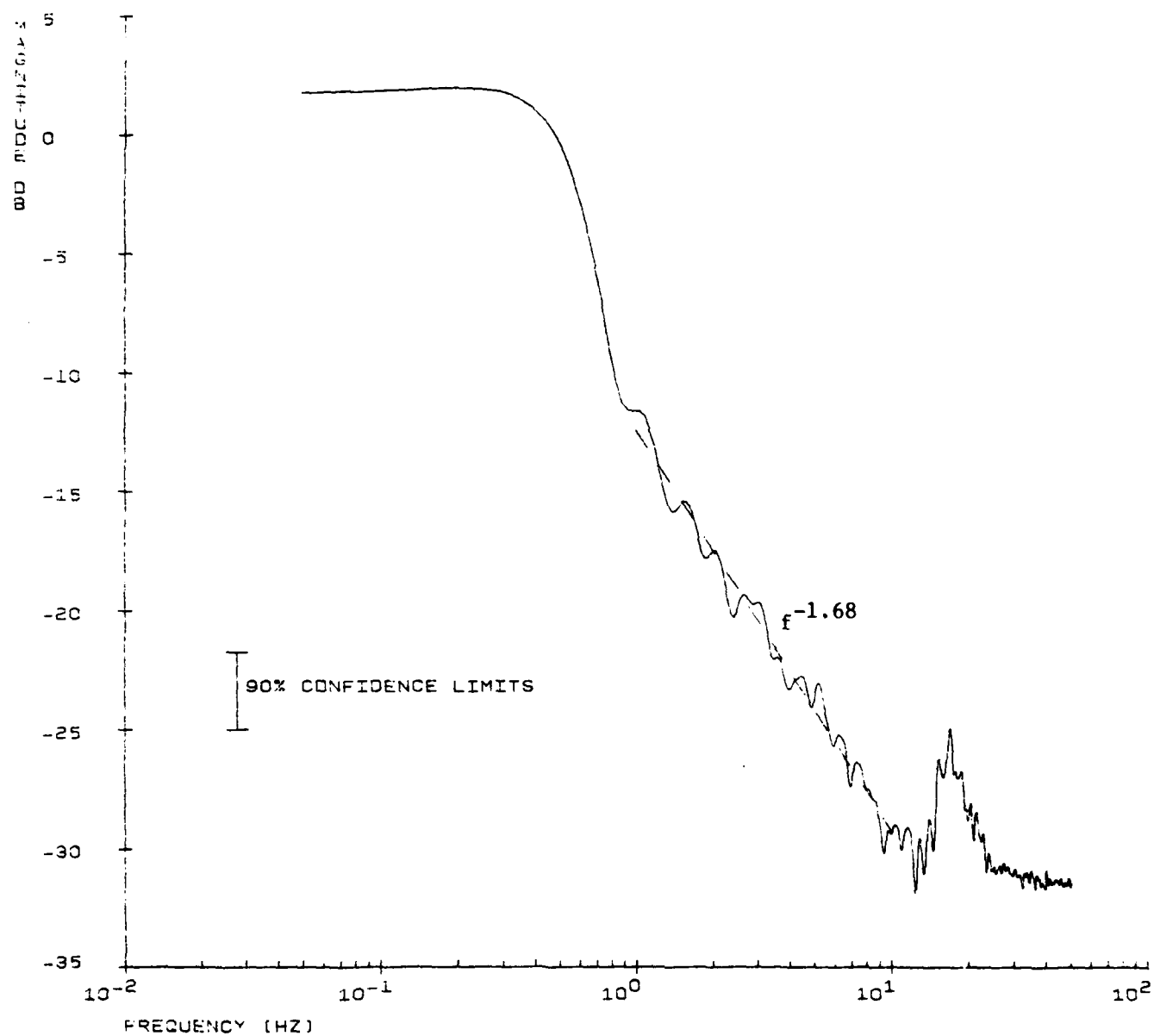
Fig. 4.4.8 Pass P3R16 Phase Spectra

PASS S1R5 POWER SPECTRA

Fig. 4.4.9 Pass S1R5 Power Spectra

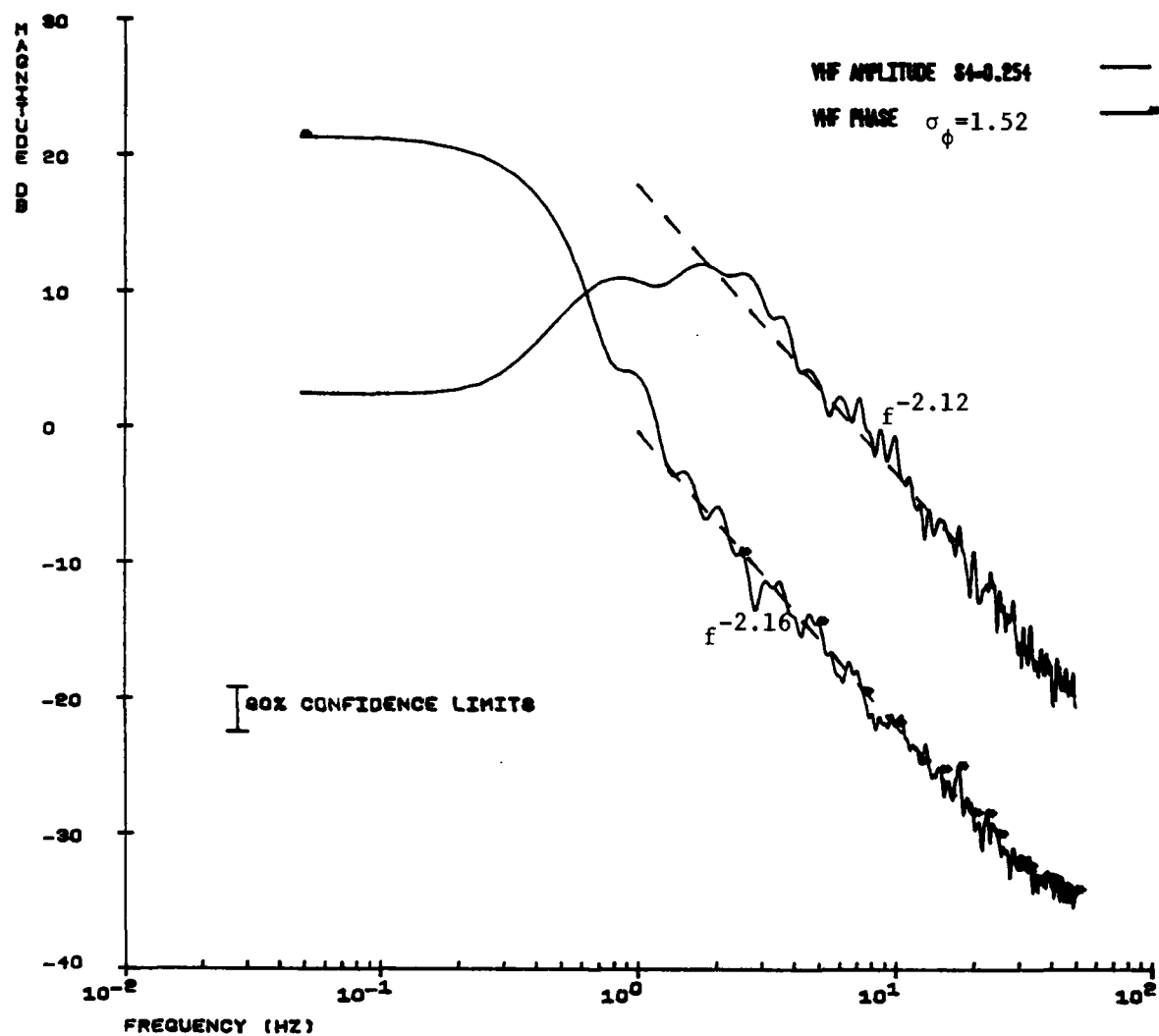Fig. 4.4.10 Pass S1R5 VHF P_L Spectrum

PASS P3 POWER SPECTRA

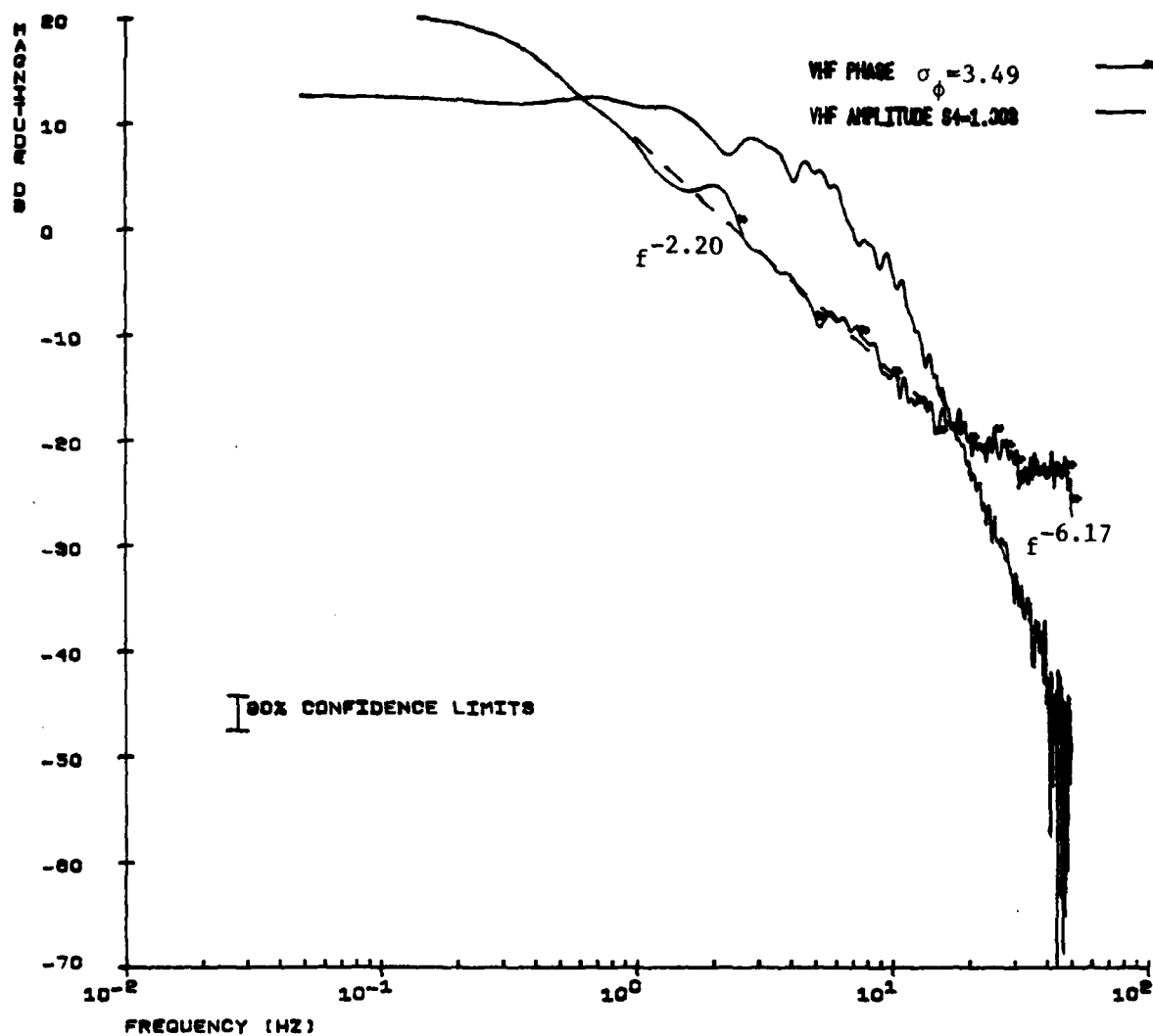Fig. 4.4.11 Pass P3 Power Spectra

PASS A4R16 POWER SPECTRA

Fig. 4.4.12 Pass A4R16 Power Spectra

The spectra for pass A4R16 can provide another interesting comparison with those of pass K2R4 (Fig. 4.4.13). Both scintillation index and standard deviation of phase are the same for these two passes which can serve to illuminate any possible geographic differences. The phase spectra are about the same. Those of the amplitude are slightly different. That for pass A4R16 is a little broader and steeper in the high frequency end. Amplitude spectra for another pair of passes, K4 (Fig. 4.4.1) and A4R13 (Fig. 4.4.5), are also very close with equal slopes. In this case the Ancon spectrum has the more clearly defined corner frequency. Because the similarity extends into the higher frequencies as well, there seems to be little spectral difference in receptions at the two equatorial stations for data sets of the same scintillation levels.

While no mid-latitude activity is strong enough to compare to that of another station, some differences between the auroral and equatorial spectra require examination. With the same level of scintillation at VHF, the amplitude power spectrum for pass A3R5 (Fig. 4.4.14) is much broader than that of pass P3R16 (Fig. 4.4.7). The phase spectra, on the other hand, are about the same.

One might acknowledge this as a geographic difference but the fact is that no comparison can really be made. Recall the results in Fig. 4.1.1. Because the Ancon scintillation is well into saturation at VHF the scintillation index is not an accurate indicator of the ionospheric turbulence. In fact, while the auroral S_4 indices decrease with increasing frequency, the S_4 values for the Ancon station remain constant or even higher at UHF than VHF. Thus, the scintillation environment at Ancon was far more severe than that at Poker Flat for these two occasions and no conclusion can be drawn with respect to geographical spectral trends from these two sets of data. No other sets with similar scintillation levels from the two locations were found in the data for further studies of geographical trends.
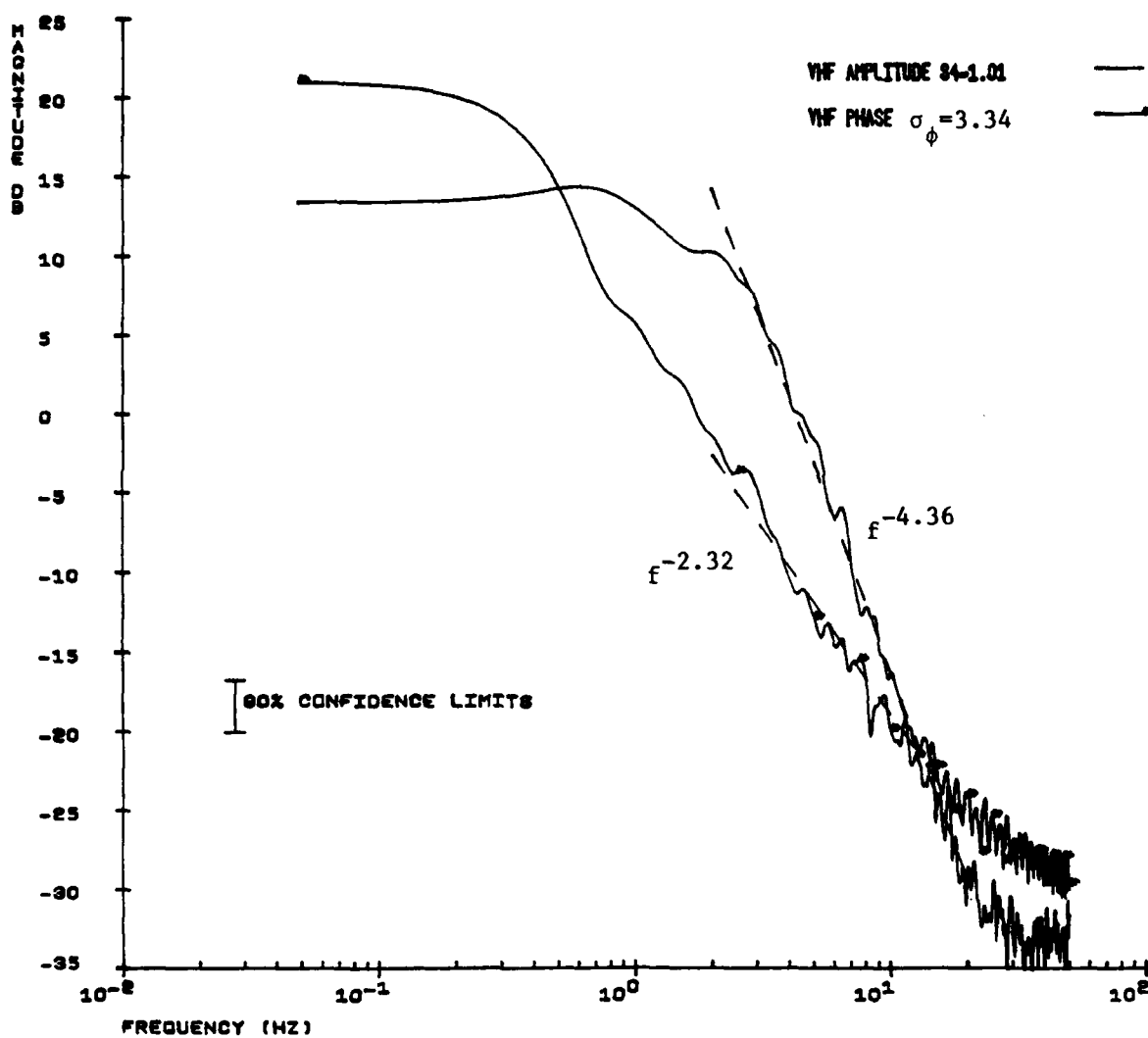
Fig. 4.4.13   Pass K2R4 Power Spectra
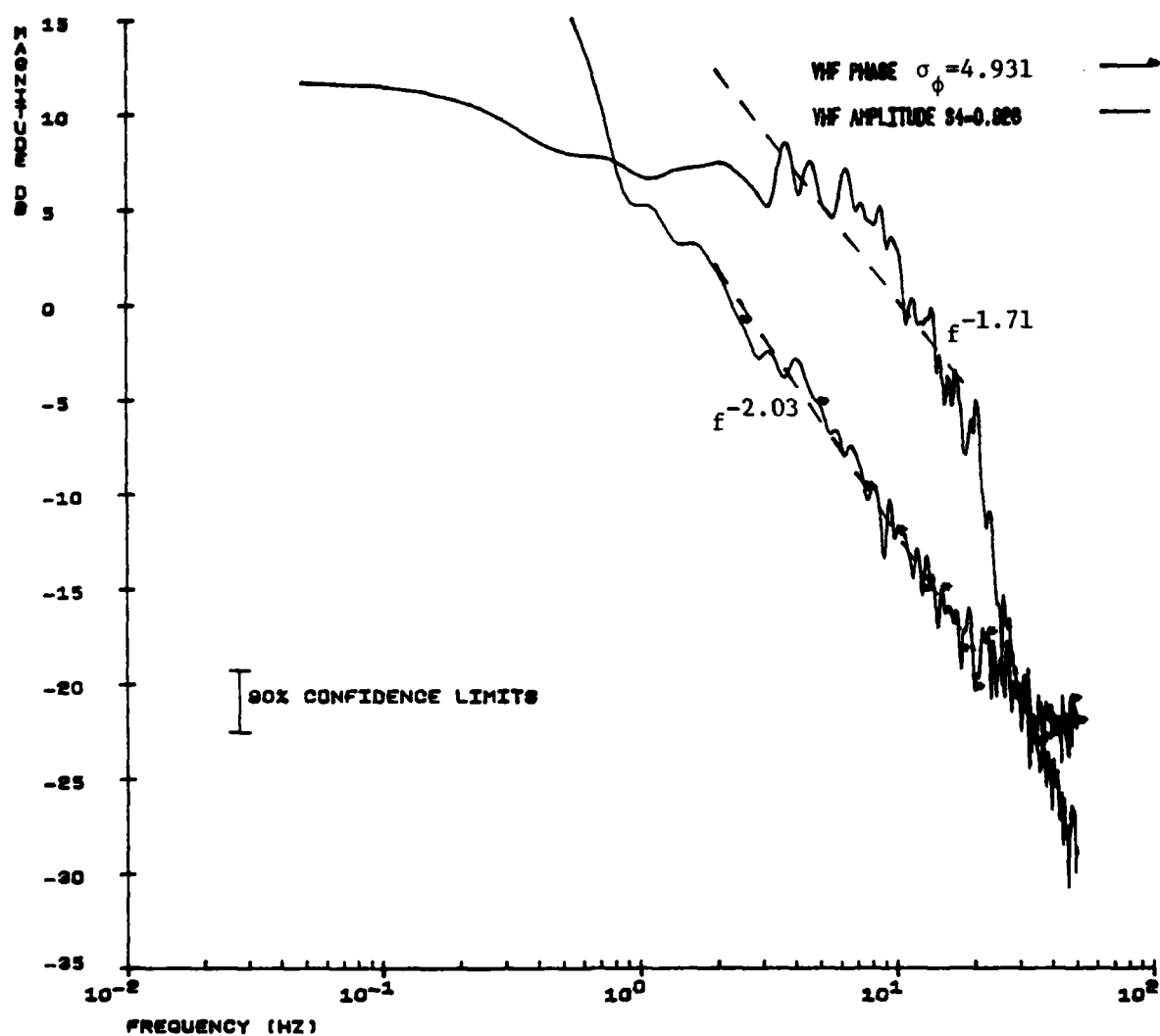
PASS A3R5 POWER SPECTRA

Fig. 4.4.14   Pass A3R5 Power Spectra

5. Summary and Conclusions

The data from the DNA Wideband Satellite Experiment provide a good basis for the study of transionospheric scintillation. Though stationary segements of data are difficult to locate, the results they provide are fairly consistent. The frequency dependence of scintillation, relationship of average field to electron density fluctuations, characteristics of the autocorrelation and spectral as well as geographic trends are all made available.

Scintillation was shown to generally increase at lower frequency. Scintillation index varied as f^{-n} with n approaching zero for saturation $(S_4 \approx 1)$. The standard deviation of the phase varied as f^{-1} but levels off for the strongest scintillation cases.

The logarithm of the squared mean field, $\ln\langle U \rangle^2$, was demonstrated to be proportional to f^{-2}. This trend was predicted theoretically in equation 4.1.8. Thus, as expected for the same patch of ionosphere, the data at different frequencies yield a constant $A_N(0)$ (defined in equation 2.3.8). Comparing different values of $A_N(0)$ with corresponding S_4 values verifies that stronger scintillation occurs when there is greater electron density fluctuation.

The correlation interval, defined as the amount of time the autocovariance remains greater than half, depends both on frequency and scintillation level. By fixing S_4 the different dependences on frequency were observed. These can be explained by the Fresnel filtering and decorrelation due to multiple scattering. The phase correlation interval remained nearly constant for weak scintillation but decreased in the presence of multiple scattering.

The effects of strong scintillation are evident in the spectral plots as well. While the amplitude spectra are broadened for very intense activity, the phase spectra become somewhat flatter. In the weak cases, as predicted theoretically, the amplitude and phase have the same spectral slope.

As predicted theoretically, the P_L spectrum should indicate the spectrum of electron density fluctuations. Its independence of carrier frequency as well as its similarity to the phase spectrum have been demonstrated. Since the phase spectrum has been used to yield information about the irregularity (Rino, 1980), the technique proves consistent.

Certain geographic trends were also shown. Scintillation is weak at temperate latitude, stronger at high latitude and extremely strong in the equatorial region. Scintillation index is highest at Ancon and Kwajalein though the standard deviation of the phase is comparable at the Poker Flat station. For both amplitude and phase scintillation, however, the Stanford data shows the weakest activity by far.

In summary, the data confirms many of the theoretical predictions. While orbiting satellite data does not always exhibit stationarity, what is used here is very valuable due to the large number of frequencies available, the high sampling rate, and the S-band phase reference. Analysis of the results in light of the various theoretical models provides insight both into the character of the scintillation as well as the ionospheric irregularities themselves.

References

Blackman, R. B. and Tukey, J. D., (1958), The Measurement of Power Spectra, Dover Publications, New York.

Crane, R. K., (1976), Spectra of Ionospheric Scintillation, Journal of Geophysical Research , 81, 2041-2050.

Fremouw, E. J., Leadabrand, R. L., Livingston, R. C., Cousins, M. D., Rino, C. L., Fair, B. C., Long, R. A., (1978), Early Results from the DNA Wideband Satellite Experiment -- Complex Signal Scintillation, Radio Science, vol. 13, no. 1, 167-187.

Lathi, B. P., (1974), Signals, Systems, and Controls, Intext Educational Publishers, New York.

Liu, C. H., Wernik, A. W., Yeh, K. C., and Youakim, M. Y., (1974), Effects of Multiple Scattering on Scintillation of Trans-Ionospheric Radio Signals, Radio Science, 9, 566-607.

Lovelace, R. V. E., Saltpeter, E. E., and Sharp, L. E., (1970), Analysis of Observations of Interplanetary Scintillations, Astrophys. J., 159, 1047-1055.

Marians, M., (1975), Computed Scintillation Spectra for Strong Turbulence, Radio Science, 10, 115-119.

Myers, W. J., Gjeldum, R. J., Liu, C. H., and Yeh, K. C., (1979), A Study of Ionospheric Scintillations of Phase and Quadrature Components, Journal of Geophysical Research, 84, 2039-2047.

Oppenheim, A. V., and Schafer, R. W., (1975), Digital Signal Processing, Prentice-Hall, Inc., New Jersey.

Rino, C. L., (1980), A Power-law Phase Screen Model for Ionospheric Scintillation 1. Weak Scatter, to appear in Radio Science.

Rufenach, C. L., (1972), Power-law Wavenumber Spectrum Deduced from Ionospheric Scintillation Observations, _Journal of Geophysical Research_, 77, 4761-4772.

Rumsey, V. H., (1975), Scintillations Due to a Concentrated Layer with a Power-law Turbulence Spectrum, _Radio Science_, 10, 107-114.

Singleton, D. G., (1974), Power Spectra of Ionospheric Scintillations, _Journal of Atmospheric Terrestrial Physics_, 36, 113-133.

Tatarski, V. I., (1971), The Effects of the Turbulent Atmosphere on Wave Propagation, U.S. Dept. of Commerce, National Technical Information Service, Springfield, Va.

Umeki, R., Liu, C. H., Yeh, K. C., (1976), Ionospheric Scintillations at Multiple Frequencies, Ionosphere Radio Laboratory, University of Illinois, Urbana, Il.

Umeki, R., Liu, C. H., Yeh, K. C., (1977a), Multifrequency Studies of Ionospheric Scintillations, _Radio Science_, 12, 311-317.

Umeki, R., Liu, C. H., Yeh, K. C., (1977b), Multifrequency Spectra of Ionospheric Amplitude Scintillations, _Journal of Geophysical Research_, 82, 2752-2759.

Wernik, A. W., Liu, C. H., Youakim, M. Y., Yeh, K. C., (1973), A Theoretical Study of Scintillation of Transionospheric Radio Signals, Ionosphere Radio Laboratory, University of Illinois, Urbana, Il.

Wernik, A. W., Liu, C. H., (1974), Ionospheric Irregularities Causing Scintillation of GHz frequency Radio Signals, _Journal of Atmospheric Terrestrial Physics_, 36, 871-879.

Yeh, K. C., Liu, C. H., and Youakim, M. Y., (1975), A Theoretical Study of the Ionospheric Scintillation Behavior Caused by Multiple Scattering, _Radio Science_, 10, 97-106.

Appendix

In this appendix data from pass P3R16 are presented. The amplitude and phase are both ten second detrended with mean set at one for amplitude and zero for phase. In addition, continuity has been restored to the phase in order to avoid any 2π ambiguity. Some information about the pass is given in Table A1 and plots at each frequency are presented in Figs. A1-A5.

TABLE A1   Pass Information

Pass: P3R16

Location: Poker Flat, Alaska

Time: day 67, 1978 18:37:10.06 UT

Duration: 40 seconds

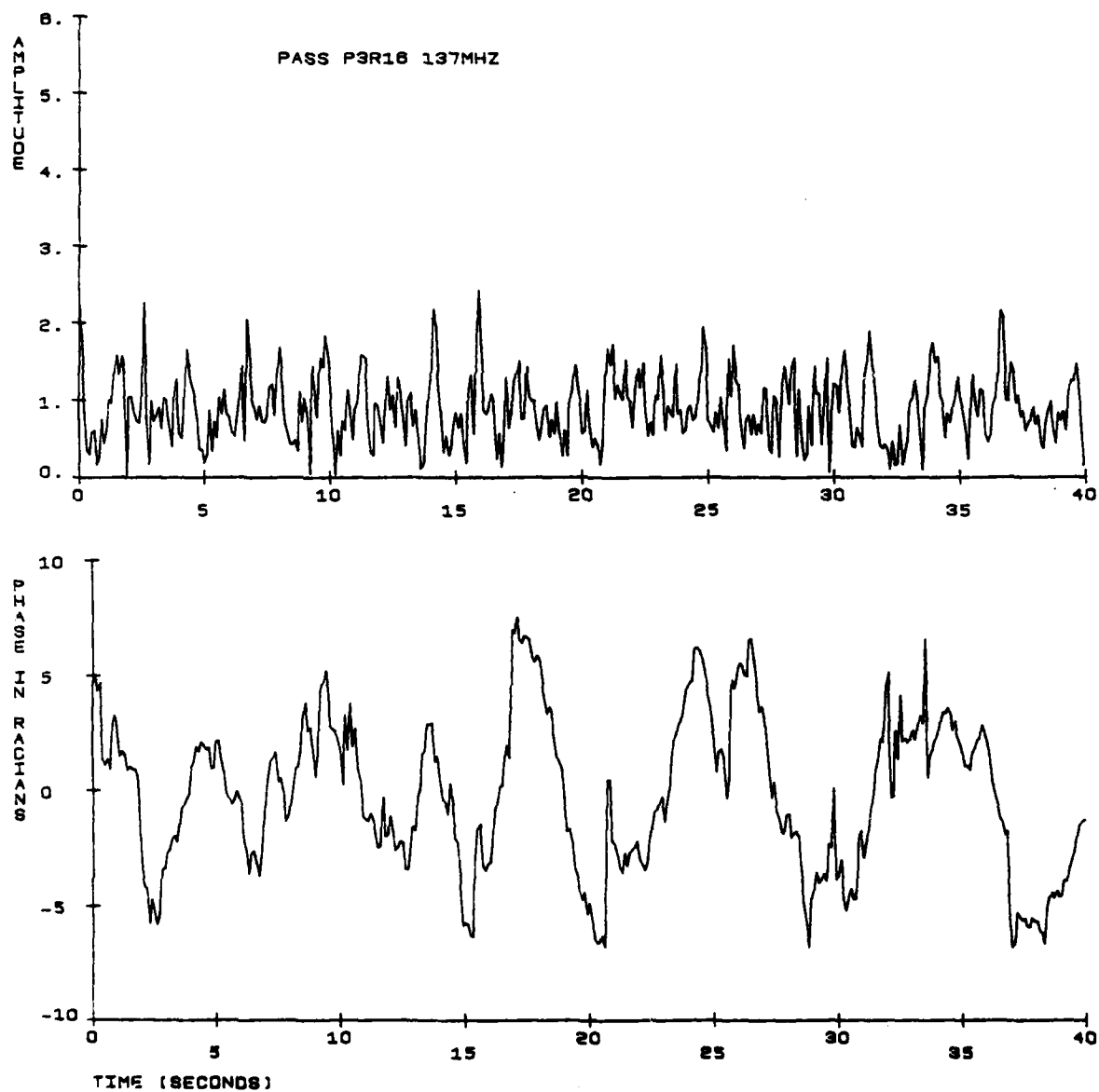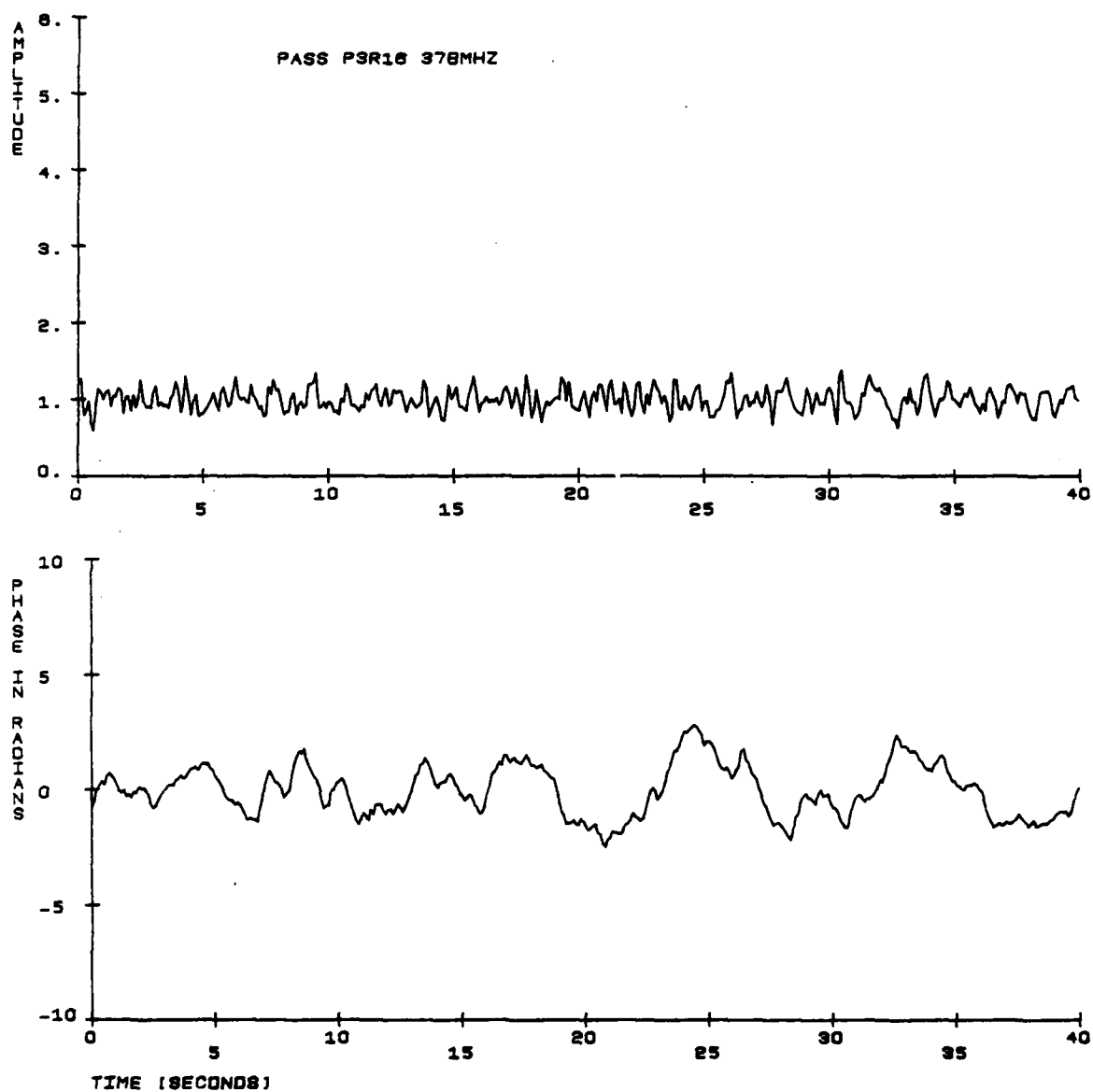| Frequency (MHz)	S_4	σ_ϕ (rad.)
137	0.917	3.33
378	0.289	1.11
447	0.228	0.940
1239	0.055	0.285
2891	0.029	0.002

Fig. Al   0.1 Hz Detrended VHF signal

Fig. A2 0.1 Hz Detrended UHF signal
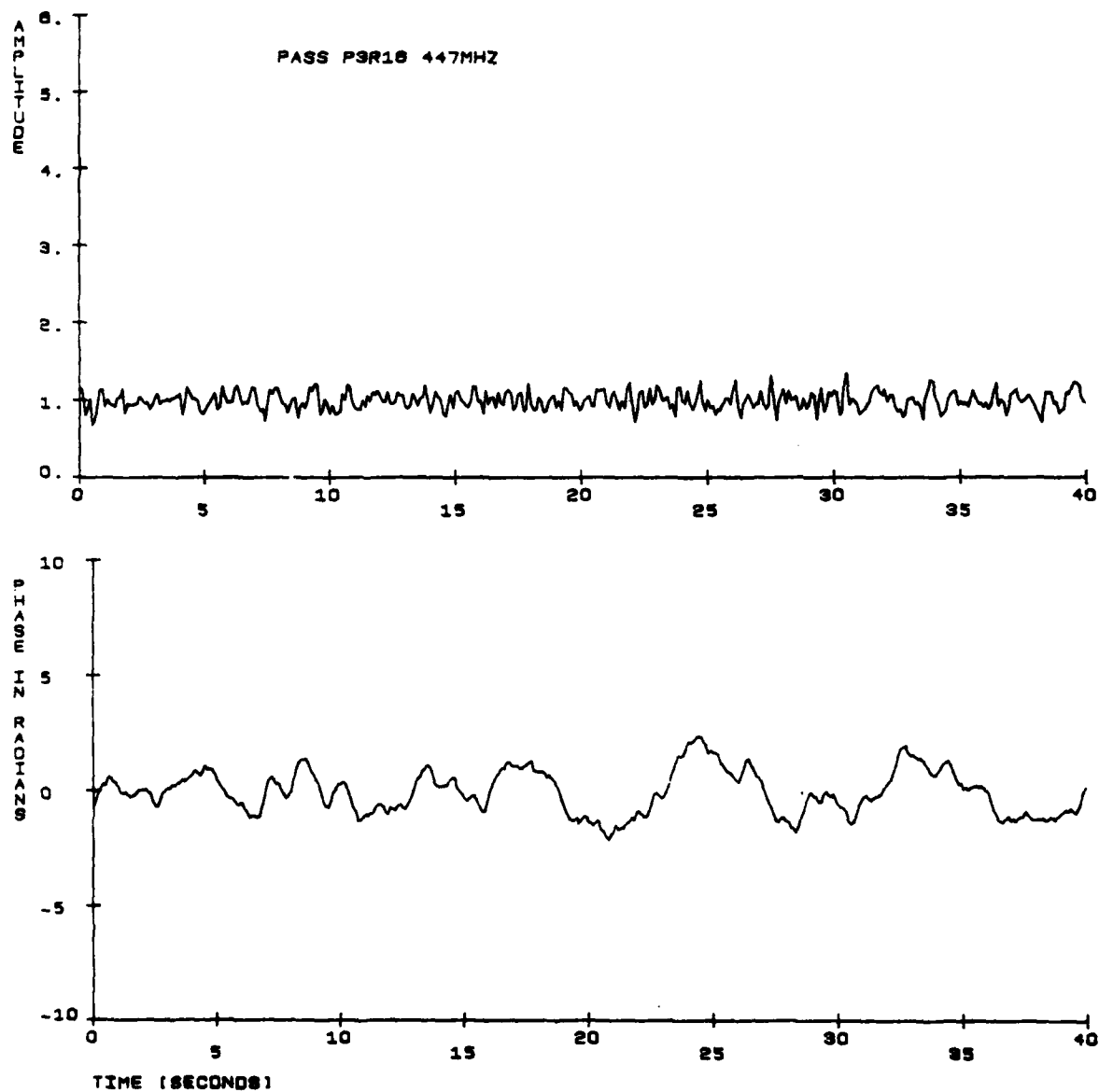
Fig. A3   0.1 Hz Detrended UHF signal
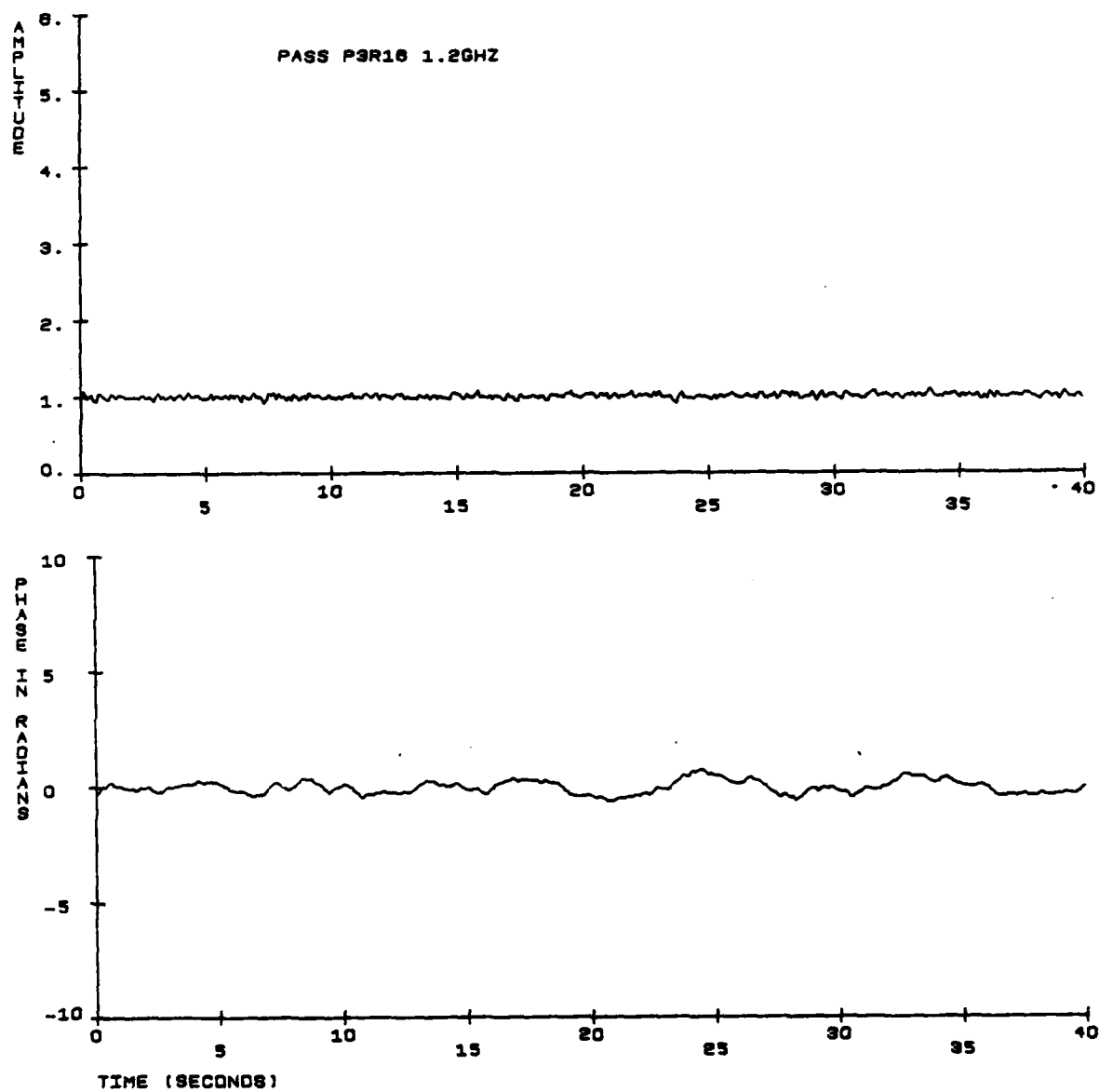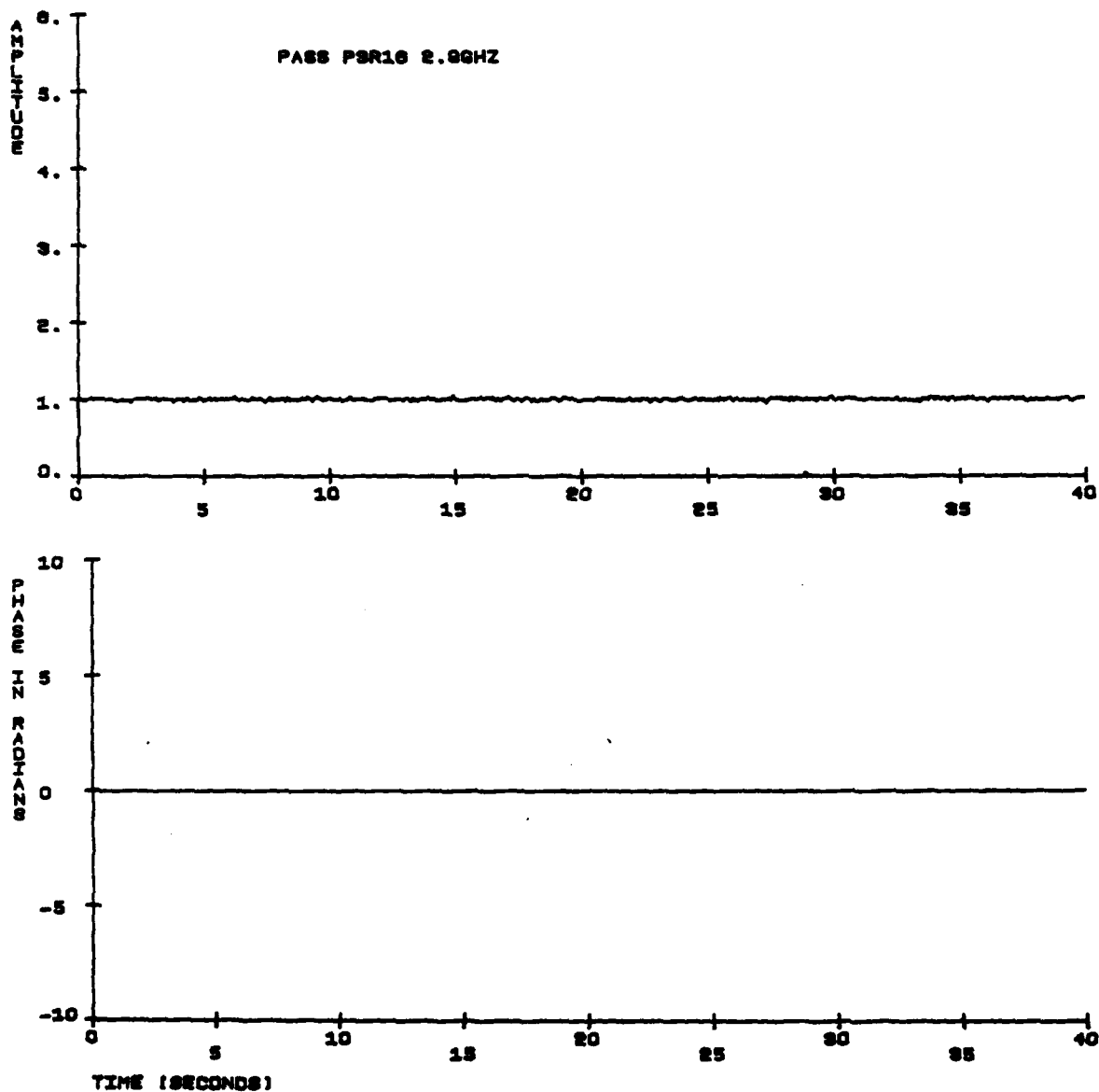
Fig. A4   0.1 Hz Detrended L-band signal

Fig. A5 0.1 Hz Detrended S-band signal

FILMED

–8